An integral framework for computational thermo-elastic homogenization of polycrystalline materials

Ivano Benedetti[a,*]

[a]*Department of Engineering, University of Palermo, Viale delle Scienze, Edificio 8, Palermo, 90128, Italy*

Abstract

A grain scale framework for thermo-elastic analysis and computational homogenization of polycrystalline materials is proposed. The morphology of crystal aggregates is represented employing Voronoi tessellations, which retain the main statistical features of polycrystalline materials. The behaviour of the individual grains is modelled starting from an integral representation for anisotropic thermo-elasticity, which is numerically addressed through a dual reciprocity boundary element method. The integrity of the aggregate is enforced through suitable intergranular thermo-elastic continuity conditions. By virtue of the features of the underlying formulation, the polycrystalline thermo-elastic problem is expressed in terms of grain boundary variables only, thus simplifying the subsequent task of meshing and reducing the overall computational cost of the analysis, ultimately providing an appealing tool for multiscale applications. The framework has been tailored for computational thermo-elastic homogenization of polycrystalline materials and it has been applied to the statistical computational homogenization of SiC and Al_2O_3 polycrystals, with accurate results confirming its robustness and effectiveness. The extension of the proposed framework to multiscale modelling of materials failure in thermally active environments is eventually discussed.

Keywords: Thermo-elasticity, Polycrystalline materials, Computational homogenization, Computational micro-mechanics, Multiscale materials modelling, Boundary element method

1. Introduction

Materials computational modelling has become an established practice in engineering and science, for both analysis and design purposes [1]. The capability to understand, model, interpret and

*Corresponding author
Email address: ivano.benedetti@unipa.it (Ivano Benedetti)

explain materials behaviours has been gradually extended, evolving from simple phenomenological modelling at a selected application scale to physically based modelling spanning several scales, and even including *ab initio*, or first principles, tools in the most inclusive applications [2].

Such evolution has been underpinned both by remarkable developments in experimental multiscale characterization of materials [3, 4, 5, 6], which make now experimentally accessible even complex phenomena at the smallest scales, and by the rapid technological progress and consequent increased affordability and availability of high performance computing [7], which has allowed the inclusion of a broader range of morphological and constitutive features in the materials model representation, making it possible to simulate complex, interacting nonlinear phenomena, e.g. damage and cracking [8, 9]. Nowadays, the convergence of multiscale experimental materials characterization, computational multiscale materials modelling and advanced manufacturing technologies, e.g. additive manufacturing or continuous tow shearing [10], is unfolding the potential of the *materials by design* paradigm [11].

This work proposes an original computational framework for thermo-elastic homogenization of polycrystalline materials, built on an explicit Voronoi representation of three-dimensional crystal aggregates and on a boundary elements model of the coupled thermo-elastic behaviour at the crystal scale. Polycrystalline materials, which include metals, ceramics and alloys, are an important class of materials with countless applications in many technological sectors, from civil to industrial engineering. Their physical properties at the component level, whose size may span the range $10^{-3} - 10^{1}$ m, depend on the features of and mutual interactions among the aggregate grains, whose individual size may range from nm (10^{-9} m) to µm (10^{-6} m).

Computational homogenization allows estimating the properties of the material at the component macro-level, where it is represented as a continuum medium, from the knowledge of the morphological and constitutive features of the material micro-constituents or phases. Such estimation is made through suitable volume averages of the strain and/or stress micro-fields, as reconstructed by solving a well-posed boundary value problem (BVP) with a certain computational method [12, 13]. While the finite element method (FEM) has often been employed as a popular computational choice in this context [14], this work proposes a different framework, based on the employment of integral equations as a starting point for the solution of the thermo-elastic polycrystalline BVP.

Computational tools based on integral equations and on the employment of the boundary element method (BEM) [15, 16] for their solution have been already successfully developed for the

analysis of polycrystalline materials, both in 2D [17] and 3D [18, 19], and have been applied to either computational homogenization [20], multiscale materials modelling [21, 22, 23] or micro-cracking analysis [24, 25, 26], also considering piezo-electric polycrystals [27], high-cycle and low-cycle fatigue [28, 29] and hydrogen assisted cracking [30]. Such formulations, often built on Voronoi tessellations [31], which provide a reasonable approximation of the microstructural morphology [32, 33], are expressed uniquely in terms of displacements and tractions of points belonging to the boundary of the crystals in the aggregate, thus providing a reduction in the number of degrees of freedom needed for analysing a give microstructure. Moreover, such *boundary-only* nature of formulation is particularly convenient, as it allows its natural coupling with cohesive zone modelling, thus providing a powerful reduced order tool for polycrystalline micro-cracking.

However, the pure boundary nature of the formulation is generally lost when volume body forces, inertial forces or more complex constitutive behaviours are considered [16]. For polycrystalline materials, this is the case when crystal plasticity [34, 35] or dynamic loading [36] are considered; it is also the case of thermo-elastic analysis, in which the constitutive thermo-elastic coupling introduces volume integrals in the boundary integral equations [37]. In some cases, such volume integrals may be re-transformed into boundary integrals, either using an *exact transformation method*, as done for example by Geraci & Aliabadi in Ref.[38], who addressed steady-state and transient thermo-elasticity in two-dimensional polycrystals, or by introducing an auxiliary approximation of the volume terms and re-applying the reciprocity theorem to such approximating terms, so as to obtain an approximated boundary representation of the volume integrals, as done by Galvis and co-workers, who applied the so-called *dual reciprocity method* (DRM) [39, 40, 41] to the analysis of dynamic cracks propagation in 2D polycrystals [36] and to the dynamic analysis of 3D polycrystals [42].

In this study, for the first time, a three-dimensional multi-region dual reciprocity boundary element formulation is developed for the thermo-elastic homogenization of three-dimensional polycrystalline materials. The formulation is based of the work by Kögl and Gaul [43], who developed a boundary element method for anisotropic coupled thermo-elasticity. The fundamental solutions of the uncoupled elasto-static and thermal steady-state operators are employed to build a dual reciprocity method for coupled anisotropic thermo-elasticity, which provides the key building block of the Voronoi-DRM polycrystalline formulation. The formulation is then applied to the direct thermo-elastic homogenization of two example polycrystalline materials, employing an original method for enforcing periodic boundary conditions on periodic non-prismatic unit cells, while removing prob-

lematic rigid body motions.

The paper is organized as follows. Section 2 introduces the digital representation of polycrystalline aggregates based on three-dimensional tessellation algorithms, an essential item for the correct morphological representation of the material microstructure. Section 3 briefly recalls the governing equations of thermo-elasticity and restricts the focus on steady-state thermo-elasticity; Section 3.1, in particular, introduces a generalized thermo-elastic notation that allow writing the thermo-elastic integral representation introduced in Section 4 in a compact format, particularly suited for computer implementation; Section 4.2 discusses the treatment of the volume integral terms originating from the thermo-elastic coupling and their transformation to boundary integrals by the DRM. Section 5 describes the boundary element discretization technique and the computational solution of the obtained discrete system of equations. The tailoring of the method to the computational thermo-elastic homogenization of polycrystals is thoroughly discussed in Section 6, while Section 7 is devoted to the statistical computational homogenization of two polycrystalline materials. Section 8 eventually discusses some limitations and subsequent possible directions for further research, before *Conclusions* are drawn.

2. Artificial morphology representation of polycrystalline specimens

The first essential step towards modelling polycrystalline specimens is the provision of a suitable morphological representation of the considered aggregates. In the literature, several different strategies have been adopted, from highly idealized, rough, morphologies to highly accurate microstructural reconstructions based on the use of sophisticated experimental techniques [44, 14].

A good compromise between mathematical and computational simplicity and morphological fidelity is provided by some well defined mathematical algorithms able to provide artificial space tessellations constituting a reasonable approximations of real polycrystalline microstructures: in this study, three-dimensional Voronoi-Laguerre tessellations are employed to build the artificial representations of crystal aggregates, as they have been proved able to retain the main statistical morphological features of polycrystals [45, 46, 33]. The morphological representation is then supplemented with a suitable crystallographic characterization, in which each grain is assigned a specific crystallographic orientation in the three-dimensional space.

In the developed model, a particularly convenient property of Laguerre-Voronoi tessellations is the fact that each cell/grain/crystal g, occupying the region Ω^g, is geometrically represented by a

convex polyhedron enclosed by the union of *flat* convex polygonal faces Γ_f^g, so that

$$\Gamma^g = \partial\Omega^g = \bigcup_{f=1}^{N_f^g} \Gamma_f^g, \tag{1}$$

where Γ_f^g is the generic *f-th* face of the *g-th* grain, with $f = 1, \ldots, N_f^g$. As it will be discussed in Section 5, this aspect provides a remarkable simplification in the discretisation and numerical treatment of the proposed boundary integral formulation.

From the operational point of view, an aggregate occupying the volume V bounded by $S = \partial V$, can be effectively generated using open source software packages such as [1]`Voro++` [47], `Neper`[2] [45] or `OptiMic`[3] [48] or other proprietary software suites such as `VoroCrust`[4] [49], developed by the Sandia National Laboratories. Such packages can be either directly or indirectly employed to tessellate either *convex* or *non-convex* volumes V, which is particularly convenient, as non-convex domains might be useful to effectively represent the geometry of polycrystalline micro-devices (micro-beams, brackets, gears, etc.) [50, 28]. Additionally, they can be employed to generate *periodic non-prismatic* tessellations, useful to remove possible boundary layer effects originating from the presence of small fractions of grains resulting from their cutting in correspondence of the domain boundary walls and thus to improve the convergence of homogenization procedures employing periodic boundary conditions, as discussed in e.g. in Ref.[20], to which the interested readers are referred for further details. Fig.(1) shows examples of a generic, non-periodic, prismatic tessellation and of a periodic non-prismatic tessellation.

3. Thermo-elasticity governing equations

The equations of elasticity, in presence of thermal loadings, may be written in tensorial notation as

$$\varepsilon_{kl} = \frac{1}{2}\left(u_{k,l} + u_{l,k}\right), \qquad \sigma_{ij} = C_{ijkl}\varepsilon_{kl} - \gamma_{ij}\theta, \qquad \sigma_{ij,j} + f_i = \rho\ddot{u}_i, \tag{2}$$

where $i, j = 1, 2, 3$, the Einstein summation convention is assumed, a comma in a subscript denotes differentiation with respect to the spatial coordinate identified by the letters following the comma

[1] `http://math.lbl.gov/voro++/`
[2] `https://neper.info/#`
[3] `https://github.com/ElsevierSoftwareX/SOFTX-D-21-00006`
[4] `https://vorocrust.sandia.gov`

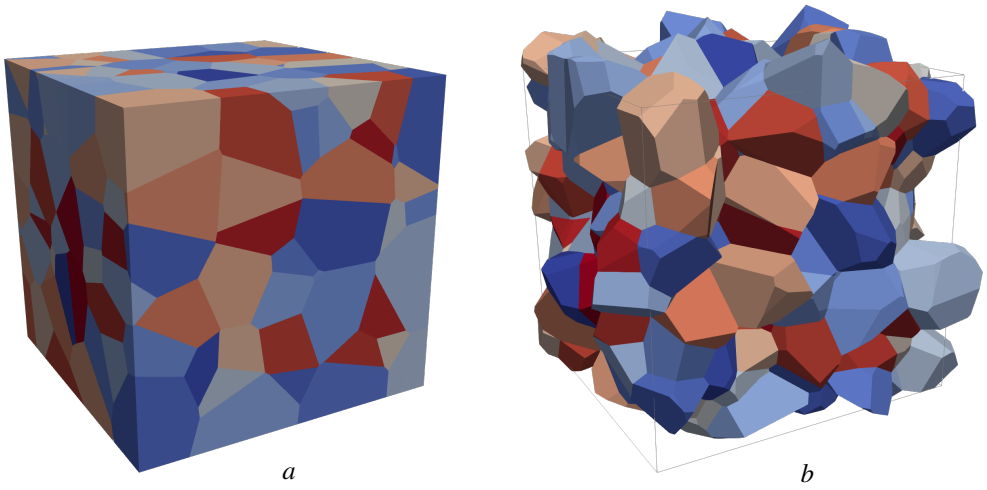

Figure 1: Example of: *a*) a 300-grain non-periodic tessellation of a prismatic domain (cube); *b*) a 300-grain periodic non-prismatic tessellation.

itself and the overdots denote time differentiation. In Eqs.(2): u_i, ε_{kl}, σ_{ij} express, respectively, the components of the displacement field, small strains tensor and Cauchy stress tensor; $\theta = \Delta T = T - T_0$ is the difference with respect to a reference temperature T_0; C_{ijkl} are the components of the fourth-order elasticity tensor, measured at constant temperature; γ_{ij} are the components of the thermo-elasticity tensor; ρ is the material mass density; f_i are components of the body force density. It is straightforward to recognise that Eqs.(2) collect the strains-displacements relations, the constitutive equations in presence of thermal loads and the momentum balance equations.

On the other hand, the equations governing the thermal evolution may be collected as

$$q_i = -k_{ij} T_{,j} = -k_{ij} \theta_{,j}, \qquad s = \gamma_{ij} \varepsilon_{ij} + \frac{c}{T_0} \theta, \qquad T \dot{s} = \omega - q_{i,i} \tag{3}$$

where q_i are the components of the heat flux vector, s is the entropy density, k_{ij} are the components of the thermal conductivity tensor, c is the volumetric heat capacity and ω is the heat source density. Eqs.(3) represent respectively *a*) the Fourier's law of heat conduction, linking the heat flux vector to the temperature field, *b*) the thermal constitutive equations, linking the entropy density to the strains and temperature difference with respect to a reference thermal status, and *c*) the local entropy balance.

Combining and suitably manipulating Eqs.(2) and Eqs.(3), the following equations of linear

anisotropic thermo-elasticity are obtained

$$\begin{cases} C_{ijkl}u_{k,lj} + f_i = \rho\ddot{u}_i + \gamma_{ij}\theta_{,j} \\ k_{ij}\theta_{,ij} + \omega = c\dot{\theta} + T_0\gamma_{ij}\dot{u}_{i,j} \end{cases} \tag{4}$$

that, for the solution of specific thermo-elastic problems, must be complemented with suitable sets of *mechanical* boundary and initial conditions

$$\text{MBCs} \quad \begin{cases} u_i(\tau) = \bar{u}_i(\tau) & \text{on } \Gamma_u \\ t_i(\tau) = \bar{t}_i(\tau) & \text{on } \Gamma_t \end{cases} \qquad \text{MICs} \quad \begin{cases} u_i(\tau = 0) = u_i^0 \\ \dot{u}_i(\tau = 0) = \dot{u}_i^0 \end{cases} \text{ in } \Omega \tag{5}$$

and *thermal* boundary and initial conditions

$$\text{TBCs} \quad \begin{cases} \theta(\tau) = \bar{\theta}(\tau) & \text{on } \Gamma_\theta \\ q(\tau) = \bar{q}(\tau) & \text{on } \Gamma_q \end{cases} \qquad \text{TICs} \quad \theta(\tau = 0) = \theta^0 \quad \text{in } \Omega \tag{6}$$

where the elastic and thermal fluxes are defined by

$$\begin{aligned} t_i(\tau) &= \sigma_{ij}n_j = C_{ijkl}u_{k,l}n_j - \gamma_{ij}n_j\theta \\ q(\tau) &= q_i n_i = -k_{ij}\theta_{,j}n_i \end{aligned} \tag{7}$$

and τ represents time.

Eqs.(4-7) model three-dimensional anisotropic fully coupled transient thermo-elastic problems, where volume body forces and heat sources are present, both inertial and transient thermal terms play a role, and the thermo-elastic coupling is bidirectional, with mechanical dissipation affecting the thermal field, through the dissipation terms $T_0\gamma_{ij}\dot{u}_{i,j}$, and temperature affecting the mechanical fields through the terms $\gamma_{ij}\theta_{,j}$. However, as discussed e.g. in Ref.[43], different simplified thermo-elastic formulations may be obtained by selectively neglecting some terms in Eqs.(4): the *theory of thermal stresses* is obtained by neglecting the dissipation terms $T_0\gamma_{ij}\dot{u}_{i,j}$; *coupled quasi-static thermo-elasticity* is obtained by neglecting the inertial terms $\rho\ddot{u}_i$; by neglecting both inertial and dissipation terms, *uncoupled, or weakly-coupled, thermo-elasticity* studied; eventually, by neglecting, besides the above terms, also the time derivative of the thermal field, *weakly coupled steady-state thermo-elasticity* is represented.

In this work, a multi-region boundary element formulation for *steady-state* thermo-elastic analysis of polycrystalline aggregates is developed and implemented. The equations governing the

behaviour of a generic anisotropic domain, representing a crystal in the polycrystalline aggregate, can thus be obtained by suitably simplifying Eqs.(4) as

$$\begin{cases} \mathscr{L}_{ik}^{el}\left(u_k\right) = \gamma_{ij}\theta_{,j} \\ \mathscr{L}^{th}\left(\theta\right) = 0 \end{cases} \tag{8}$$

where

$$\begin{aligned} \mathscr{L}_{ik}^{el}\left(\cdot\right) &= C_{ijkl}\left(\cdot\right)_{,lj} = C_{ijkl}\frac{\partial^2\left(\cdot\right)}{\partial y_l \partial y_j} \\ \mathscr{L}^{th}\left(\cdot\right) &= k_{ij}\left(\cdot\right)_{,ij} = k_{ij}\frac{\partial^2\left(\cdot\right)}{\partial y_i \partial y_j} \end{aligned} \tag{9}$$

represent the elasto-static and steady thermal conductivity second-order linear differential operators respectively. The accompanying boundary conditions are given in Eqs.(5-6), where τ now represents an ordering parameter used to express a quasi-static evolution of the boundary loading terms, while initial conditions are no relevant for stationary problems. No external force or heat volume sources are considered, although they could be numerically treated as in Ref.[43].

3.1. Generalized thermo-elasticity notation

In the proposed integral formulation for thermo-elastic problems, it may be convenient to resort to the definition of *generalized thermo-elastic displacements* U_I and *tractions* T_I, with $I = 1, \ldots, 4$, defined as

$$U_I = \left[\begin{array}{c} \{u_i\} \\ \theta \end{array}\right] = \left\{\begin{array}{ll} u_i & I = i \leq 3 \\ \theta & I = 4 \end{array}\right. , \qquad T_I = \left[\begin{array}{c} \{t_i\} \\ q \end{array}\right] = \left\{\begin{array}{ll} t_i & I = i \leq 3 \\ q & I = 4 \end{array}\right. , \tag{10}$$

which allow a compact expression of the integral equations for thermo-elastic analysis.

An essential item in such integral equations are the *fundamental solutions*, which appear as kernels in the integrand expressions. The proposed formulation employs the fundamental solutions of three-dimensional fully anisotropic and *uncoupled* elasto-static and steady-state thermal conductivity operators, i.e. the solutions $u_{ij}^{*}\left(\boldsymbol{x}, \boldsymbol{y}\right)$ and $\theta^{*}\left(\boldsymbol{x}, \boldsymbol{y}\right)$ of the following uncoupled differential systems

$$\begin{aligned} \mathscr{L}_{jr}^{el}\left(u_{ir}^{*}\right) + \delta_{ji}\,\delta\left(\boldsymbol{x}, \boldsymbol{y}\right) = 0 \\ \mathscr{L}^{th}\left(\theta^{*}\right) + \delta\left(\boldsymbol{x}, \boldsymbol{y}\right) = 0 \end{aligned} \tag{11}$$

and the associated fundamental tractions $t_{ij}^{*}\left(\boldsymbol{x}, \boldsymbol{y}\right)$ and thermal flux $q^{*}\left(\boldsymbol{x}, \boldsymbol{y}\right)$ defined by

$$\begin{aligned} t_{ij}^{*} &= C_{jkrs}u_{ir,s}^{*}n_k = \bar{\mathscr{L}}_{jr}^{el}\left(u_{ir}^{*}\right) \\ q^{*} &= -k_{ij}\theta_{,j}^{*}n_i = \bar{\mathscr{L}}^{th}\left(\theta^{*}\right) \end{aligned} \tag{12}$$

where $i,j,k,r,s = 1,2,3$, the differentiations in the operators $\mathscr{L}^{el}_{jr}\left(u^*_{ir}\right) = C_{jkrs}u^*_{ir,sk}$, $\mathscr{L}^{th}\left(\theta^*\right) = k_{ij}\theta_{,ij}$ and in the flux operators $= \bar{\mathscr{L}}^{el}_{jr}\left(\cdot\right) = C_{jkrs}n_k\partial\left(\cdot\right)/\partial y_s$ and $\bar{\mathscr{L}}^{th}\left(\cdot\right) = -k_{ij}n_i\partial\left(\cdot\right)/\partial y_j$ are taken with respect to the variables y_k, $\delta\left(\boldsymbol{x},\boldsymbol{y}\right)$ is the Dirac's delta function *collocated* at the source point $\boldsymbol{x}$ and δ_{ij} is the Kronecker delta. In the vectorial case, the generic fundamental solution component $f^*_{ij}\left(\boldsymbol{x},\boldsymbol{y}\right)$ is the *j-th* component of the considered field at the point $\boldsymbol{y}$ when the source point is loaded along the *i-th* direction at the point $\boldsymbol{x}$; in the scalar case, the subscripts are not needed, and the fundamental solutions express values at $\boldsymbol{y}$ when the source is at $\boldsymbol{x}$. Further details about the computation of the fundamental solutions are given in Appendix A.

If the generalized notation is adopted, the components of the above elastic and thermal fundamental solutions may be collected as

$$U^*_{IJ} = \begin{bmatrix} \left\{u^*_{ij}\right\} & \{0\} \\ \{0\} & -\theta^* \end{bmatrix}, \qquad T^*_{IJ} = \begin{bmatrix} \left\{t^*_{ij}\right\} & \{0\} \\ \{0\} & -q^* \end{bmatrix}, \tag{13}$$

which would be the solution of the following generalized thermo-elastic differential system

$$\mathscr{L}^{\,te}_{JR}\left(U^*_{IR}\right) + \delta_{JI}\,\delta\left(\boldsymbol{x},\boldsymbol{y}\right) = 0 \tag{14}$$

where

$$\mathscr{L}^{\,te}_{IJ}\left(\cdot\right) = \begin{bmatrix} \left\{\mathscr{L}^{el}_{ij}\left(\cdot\right)\right\} & \{0\} \\ \{0\} & -\mathscr{L}^{th}\left(\cdot\right) \end{bmatrix}, \tag{15}$$

with $I,J = 1,\ldots,4$ and $i,j = 1,2,3$ and $\mathscr{L}^{\,te}_{IJ}\left(\cdot\right)$ identifying a generalized thermo-elastic differential operator.

It is worthing underlying again that, in the present approach, u^*_{ij} and t^*_{ij}, on one side, and θ^* and q^*, on the other side, are respectively associated with a static elastic and a steady thermal problem uncoupled from each other. Thus, in the above form, the terms U^*_{IJ} and T^*_{IJ} do not allow expressing the *coupled* thermo-elastic integral equations as a generalization of their elastic counterparts. For such a purpose, it is useful to introduce the generalized fundamental fluxes

$$\hat{T}^*_{IJ} = \begin{bmatrix} \left\{t^*_{ij}\right\} & \left\{-u^*_{ij}\gamma_{jk}n_k\right\} \\ \{0\} & -q^* \end{bmatrix}, \tag{16}$$

which, as it will be shown in the next section, will introduce in the integral equations the thermo-elastic coupling through the terms $\hat{T}^*_{i4} = -u^*_{ij}\gamma_{jk}n_k$, with $i = 1,2,3$, and through the presence of derivatives of θ in some volume integrals appearing in the elastic integral equations; the over-hat

in $\hat{T}^*_{IJ}$ signals precisely the presence of the coupling terms $\hat{T}^*_{i4}$ and it is employed to distinguish $\hat{T}^*_{IJ}$ from T^*_{IJ} defined in Eqs.(13), as both such tensors will be employed in the integral formulation.

The employment of generalized displacements, tractions and fundamental solutions will noticeably simplify the expression of the thermo-elastic integral equations, allowing a compact form particularly suited for computer implementation, analogous to that often used in the treatment of piezoelectric problems, see e.g. Refs.[51, 27].

4. Boundary integral formulation for thermo-elastic analysis of polycrystals

In this section, the boundary integral formulation for thermo-elastic polycrystalline analysis is developed. The method is based on the use of integral equations for the description of the thermo-mechanical behaviour of individual grains, whose morphology is digitally represented by Laguerre-Voronoi tessellations, as discussed in Section 2. The integrity of the aggregate is retrieved through suitable generalized intergranular conditions. Several scholars have addressed different aspects of the thermo-elastic analysis of solids by boundary integral methods [52, 53, 54, 55, 56, 57, 58, 59]. In this work, the approach developed for 3D anisotropic thermo-elasticity by Kögl & Gaul [43] is adopted. An important aspect is related with the appearance, in the integral equations, of terms requiring volume integration; their presence, induced by the thermo-elastic coupling, might reduce the appeal of the integral approach. However, a pure *boundary* integral representation is retrieved employing the *dual reciprocity method* (DRM), originally developed to deal with inertial terms in elastodynamics [39].

4.1. Thermo-elastic integral equations for the individual grains

The integral representation of the microstructural thermo-elastic problem for a generic individual grain $g \leq N_g$, where N_g is the number of grains in the analysed aggregate, may be expressed in terms of the generalized thermo-elastic variables defined in Section 3.1 as

$$c_{ij}\left(\boldsymbol{x}\right) U_j\left(\boldsymbol{x}\right) + \int\!\!\!\!\!\!\diagup_{\Gamma^g} \hat{T}^*_{ij}\left(\boldsymbol{x},\boldsymbol{y}\right) U_j\left(\boldsymbol{y}\right) d\Gamma_y = \int_{\Gamma^g} U^*_{ij}\left(\boldsymbol{x},\boldsymbol{y}\right) T_j\left(\boldsymbol{y}\right) d\Gamma_y + \\ + \int_{\Omega^g} U^*_{ij}\left(\boldsymbol{x},\boldsymbol{y}\right) F_j\left(\boldsymbol{y}\right) d\Omega_y \qquad i,j = 1,...,4, \tag{17}$$

which links the generalized displacement components $U_j\left(\boldsymbol{x}\right)$ at a generic *collocation point* $\boldsymbol{x} \in \Gamma^g$ with the grain boundary generalized displacements $U_j\left(\boldsymbol{y}\right)$ and tractions $T_j\left(\boldsymbol{y}\right)$, where $\boldsymbol{y} \in \Gamma^g$

is the generic *integration point* spanning the grain boundary in the integration procedure. In Eq.(17), $U_{ij}^{*}(\boldsymbol{x},\boldsymbol{y})$ and $\hat{T}_{ij}^{*}(\boldsymbol{x},\boldsymbol{y})$ are the components of the generalized 3D anisotropic thermo-elastic fundamental solutions introduced in Section 3.1 and detailed in Appendix A, computed with reference to the *g-th* grain's material, i.e. considering the material constants associated with the grain g in Eqs.(11-12); $\tilde{c}_{ij}(\boldsymbol{x})$ are *free terms*, arising from the boundary limiting procedure and depend on the smoothness of the boundary Γ^{g} at the collocation point $\boldsymbol{x}$; the symbol $\oint$ denotes the Cauchy principal value of the integral, which identifies the value of the improper integral induced by the fact that the collocation point belongs to the domain of integration, $\boldsymbol{x} \in \Gamma^{g}$; the subscript y in $d\Gamma_y$ and $d\Omega_y$ indicates that the integration is performed with respect to $\boldsymbol{y}$; eventually, $F_j(\boldsymbol{y})$ represents the components of the volume force terms induced by the thermo-elastic coupling that, for steady-state thermo-elastic problems, are defined as

$$\{F_I\} = \begin{bmatrix} \{-\gamma_{ij}\theta_{,j}\} \\ 0 \end{bmatrix} \tag{18}$$

with $I = 1,\ldots,4$, $i,j = 1,2,3$.

It is worth noting that, as anticipated in Section 3.1, the fundamental traction kernels appearing in Eq.(17) are the components $\hat{T}_{ij}^{*}(\boldsymbol{x},\boldsymbol{y})$, defined in Eq.(16), i.e. those containing the coupling thermo-elastic terms $\hat{T}_{i4}^{*} = -u_{ij}^{*}\gamma_{jk}n_k$. The specific form of the thermo-elastic boundary integral equations in Eq.(17) derives from the fact that the fundamental solutions of the uncoupled elastic and thermal problems are employed in the formulation; further details about their derivation, either from a weighted residuals or from reciprocity statements, can be found in Refs. [15, 60, 16, 43].

As mentioned above, the presence of volume integrals, also arising from the thermo-elastic coupling, makes the numerical integration of Eq.(17) more demanding with respect to problems involving boundary integrals only, e.g. elastic or piezoelectric ones, thus partially reducing the attractiveness of the integral formulation. However, such volume integrals may be transformed into boundary integrals by employing the dual reciprocity method, as details in the next section.

4.2. Volume integrals transformation by the dual reciprocity method

The transformation of the volume integrals appearing in Eq.(17) into boundary integrals may be performed exploiting the following reciprocity statement

$$\int_{\Omega^g} U_{ij}^{*} F_j d\Omega_y + \int_{\Gamma^g} U_{ij}^{*}\tilde{T}_j d\Gamma_y = \oint_{\Gamma^g} T_{ij}^{*}\tilde{U}_j d\Gamma_y + c_{ij}\tilde{U}_j(\boldsymbol{x}) \qquad i,j = 1,...,4, \tag{19}$$

where the explicit expression of the functional dependencies has been dropped, for the sake of brevity, and $\tilde{U}_I$ and $\tilde{T}_I$ are displacement and traction *particular solutions* associated with the generic volume density terms F_j obtained by solving the system

$$\mathscr{L}_{ji}^{te}\left(\tilde{U}_i\right) + F_j = 0 \tag{20}$$

with $i, j = 1, \ldots, 4$, and evaluating the associate fluxes as $\tilde{T}_j = \bar{\mathscr{L}}_{ji}^{te}\left(\tilde{U}_i\right)$.

The reciprocity statement in Eq.(19) can be effectively exploited only if the particular solutions are known, i.e. if system (20) may be analytically solved, which is not the case for generic body volume terms F_j. Additionally, in the present thermo-elastic case, F_j is a function of the derivatives of the *unknown* field U_i, see Eq.(18), which thus requires additional considerations. The *dual reciprocity method*, as proposed in Ref.[39] for elastodynamics and developed in Ref.[43] for anisotropic thermo-elastic problems, is based on the expression of the volume density terms F_j as a linear superposition of *known* tensorial radial basis functions $\tilde{F}_{jk}^s$ for which the primitives with respect to the thermo-elastic operators, i.e. the solutions of Eq.(20), can be analytically evaluated. More specifically, it is assumed that

$$F_j\left(\boldsymbol{y}\right) \approx \sum_{n=1}^{N_s} \tilde{F}_{jk}^s \alpha_k^s = \sum_{n=1}^{N_s} \tilde{F}_{jk}\left(\boldsymbol{x}_s, \boldsymbol{y}\right) \alpha_k^s \tag{21}$$

where $j, k = 1, \ldots, 4$, α_k^s are unknown coefficients to be suitably determined, $\tilde{F}_{jk}^s$ are tensorial radial basis components associated with a generic source $\boldsymbol{x}_s$, with $s = 1, \ldots, N_s$, such that

$$\mathscr{L}_{ji}^{te}\left(\tilde{U}_{ik}^s\right) + \tilde{F}_{jk}^s = 0 \tag{22}$$

and $\tilde{T}_{jk}^s$ are the associated tractions; both $\tilde{U}_{jk}^s$ and $\tilde{T}_{jk}^s$ may be expressed ad function of the Euclidean distance $r\left(\boldsymbol{x}_s, \boldsymbol{y}\right)$.

Indeed, considering the fully anisotropic nature of the thermo-elastic differential operator $\mathscr{L}^{te}\left(\cdot\right)$, finding functions $\tilde{F}_{jk}^s$ for which Eq.(22) can be analytically computed is not possible. The issue is circumvented by adopting an *inverse* approach, i.e. by assuming a *known* radial basis form for the tensorial components $\tilde{U}_{jk}^s$ and then evaluating $\tilde{T}_{jk}^s$ and $\tilde{F}_{jk}^s$ by derivation: the procedure is detailed in Appendix B, where also the analytic form adopted in this work for $\tilde{U}_{jk}^s$, $\tilde{T}_{jk}^s$ and $\tilde{F}_{jk}^s$ is given. The calculation of $\tilde{F}_{jk}^s$ is important for the subsequent expression of the unknown coefficient α_k^s in terms of the unknown nodal values of the generalized displacements, which will allow the numerical solution of the problem, see Section 5.3.

Adopting the approximation (21) into Eq.(19) eventually results in the following boundary integral representation of the volume terms

$$\int_{\Omega^g} U_{ij}^* F_j d\Omega_y = \sum_{s=1}^{N_s} \alpha_k^s \int_{\Omega^g} U_{ij}^* \Psi_{jk}^s d\Omega_y = \sum_{s=1}^{N_s} \left[c_{ij} \tilde{U}_{jk}^s (\boldsymbol{x}) + \oint_{\Gamma^g} T_{ij}^* \tilde{U}_{jk}^s d\Gamma_y - \int_{\Gamma^g} U_{ij}^* \tilde{T}_{jk}^s d\Gamma_y \right] \alpha_k^s, \tag{23}$$

which, replaced into Eq.(17), provides the boundary integral representation of the thermo-elastic problem

$$\begin{aligned} c_{ij} U_j (\boldsymbol{x}) + \oint_{\Gamma^g} \hat{T}_{ij}^* U_j d\Gamma_y - \int_{\Gamma^g} U_{ij}^* T_j d\Gamma_y = \\ = \sum_{s=1}^{N_s} \left[c_{ij} \tilde{U}_{jk}^s (\boldsymbol{x}) + \oint_{\Gamma^g} T_{ij}^* \tilde{U}_{jk}^s d\Gamma_y - \int_{\Gamma^g} U_{ij}^* \tilde{T}_{jk}^s d\Gamma_y \right] \alpha_k^s, \end{aligned} \tag{24}$$

where $i, j, k = 1, \ldots, 4$. Few observations are worthwhile about the above representation. First, the above equations must be used with reference to the specific grain g considered within the aggregate, which implies that the material constants used to compute the fundamental solutions appearing in them are referred to the grain's material. Thus, the continuity of the aggregate at the interface between two grains should be suitably enforced, see Section 4.3. It is then important to realise that the unknown fields are the grain boundary displacements and tractions U_j and T_j, while the fundamental solutions U_{ij}^*, T_{ij}^*, $\hat{T}_{ij}^*$ and the particular solutions $\tilde{U}_{jk}^s$, $\tilde{T}_{jk}^s$ all have known analytical expressions. Also, it should be noted that both the fundamental tractions components T_{ij}^* and $\hat{T}_{ij}^*$ appear in the equations. Eventually, as already mentioned, the solution of the equation requires expressing the unknown coefficients of the approximation in Eq.(21) as a function of the unknown generalized displacements, i.e. $\boldsymbol{\alpha} = \phi(\mathbf{U})$, in vector notation; the numerical strategy used for achieving this will be described in Section 5.

4.3. Intergranular continuity

The intergranular continuity conditions are enforced, considering couples of homologous nodes at the interface between two generic crystals a and b, through the equations

$$\left\{ \begin{array}{l} \check{u}_i^a + \check{u}_i^b = 0 \\ \theta^a - \theta^b = 0 \end{array} \right. , \qquad \left\{ \begin{array}{l} \check{t}_i^a - \check{t}_i^b = 0 \\ q^a + q^b = 0 \end{array} \right. \tag{25}$$

where the symbol $\check{}$ denotes components expressed in local reference systems attached to each grain face, see Fig.(2), introduced to allow the distinction between face-normal and face-tangential mechanical components. The interested readers are referred to Refs.[18, 20, 27] for further details.

5. Boundary element numerical integration and discrete system solution

For the effective solution of the microstructural thermo-elastic problem, the generalized boundary integral equations, Eqs.(24), and the associated interface conditions, Eqs.(25), must be suitably implemented. The steps for the discretization of the continuum integral equations and the solution of the resulting algebraic system are discussed in this section.

5.1. Meshing of the artificial micro-morphologies

Since only boundary integrals appear in Eqs.(24), their numerical discretization requires the creation of a mesh of the grains surfaces only, as long as the assumption of linear constitutive behaviour of the crystal interiors hold and no crystal plastic slips are activated. The possibility of studying the polycrystalline mechanics employing boundary grids only provides a relevant benefit for the computational analysis, also enhancing its robustness, as it noticeably simplifies the generation of quality meshes that, considering the statistical nature of Voronoi-Laguerre tessellations, would otherwise require specific time-consuming checks from the analyst. In this work, the grains surface meshing is performed following the procedure detailed in Ref.[20], illustrated in Fig.(2b), and briefly recalled below.

As mentioned in Section 2, polycrystalline aggregates are here represented through Laguerre-Voronoi tessellations, which collect convex polyhedral grains g bounded by flat convex polygonal faces Γ_f^g, see Eq.(1). In the discretization procedure, each face Γ_f^g is subdivided into a set of non-overlapping triangular or quadrangular, continuous and semi-discontinuous elements e_k^{gf}, so that

$$\Gamma_f^g = \bigcup_{k=1}^{N_e^{gf}} e_k^{gf}, \tag{26}$$

with e_k^{gf} being the *k-th* boundary finite element of the *f-th* face of the *g-th* grain, with $k = 1, \ldots, N_e^{gf}$. Each element e_k^{gf} is characterised by its *geometrical* vertices $\boldsymbol{y}_n^{e_k}$ and *functional* nodes $\boldsymbol{x}_n^{e_k}$, which coincide for continuous elements and differ for discontinuous ones. Semi-discontinuous elements are employed in proximity of the face's edges, to avoid well-known complexities arising in boundary element formulations when the surface normal can not be unambiguously defined at a node [61], as in the case of nodes collocated on grains edges, where two contiguous faces meet, see Ref.[20] for further details. The collection of all the elements e_k^{gf}, and their associated nodes $\boldsymbol{x}_s^{e_k}$, for all the faces f of all the grains g of the considered tessellation, constitute the boundary

element mesh over which the numerical integration of Eqs.(24) is performed, as described in the next section.

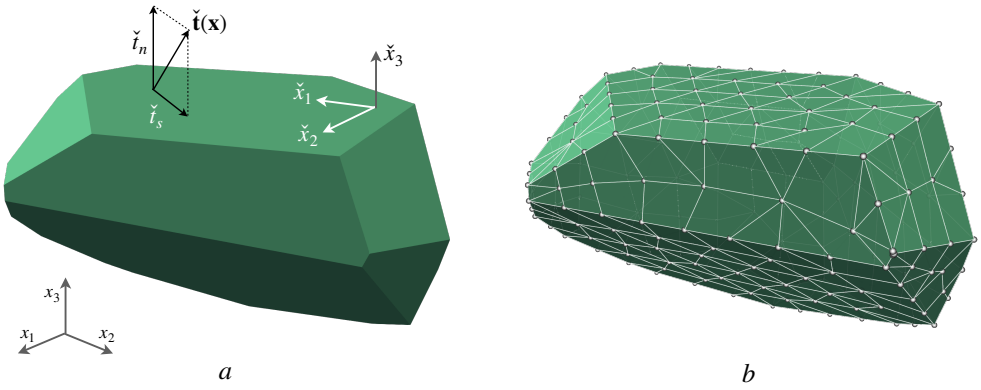

Figure 2: Example grain morphology and mesh: *a*) each grain is a convex polyhedron bounded by flat convex polygonal faces; each face carries its own local reference system $\{\tilde{x}_1\tilde{x}_2\tilde{x}_3\}$, differing from the global reference system $\{x_1x_2x_3\}$, which allows the decomposition of boundary displacements and tractions into normal and tangential components; *b*) each grain face is meshed into non-overlapping triangular or quadrangular elements.

5.2. Numerical integration of the boundary integral equations

Once an artificial tessellation and its suitable boundary elements discrezation are available, the computational treatment of the polycrystalline problem is addressed according to the following scheme.

For each grain of the aggregate, Eqs.(24) are collocated at the functional node $\boldsymbol{x}_n$ associated with the boundary element mesh. Considering the grain boundary decomposition in Eqs.(1-26), each of the integrals appearing in Eqs.(24) may be expressed as

$$\int_{\Gamma^g} F^*_{ij} V_j d\Gamma_y = \sum_{f=1}^{N^g_f} \int_{\Gamma^g_f} \check{F}^*_{ij} \check{V}_j d\Gamma_y = \sum_{f=1}^{N^g_f} \sum_{k=1}^{N^{gf}_e} \int_{e^{gf}_k} \check{F}^*_{ij} \check{V}_j d\Gamma_y, \tag{27}$$

where each of the integrals in the summation is defined over a flat two-dimensional domain, either a face or element. The terms F^*_{ij} represent the components of the generic kernels appearing in Eqs.(24), while V_j represent the components of the generic integrated field, be it either the unknown

displacements/tractions or the known particular solutions. The over check $\check{\cdot}$ indicates that the corresponding components are expressed in the local face reference systems, defined over *each* face, obtained by the transformation $V_j = R^{gf}_{jk}\check{V}_k$, with R^{gf}_{jk} indicating the components of the transformation matrix associated with the considered grain face.

Over each boundary element, the coordinates of the generic integration point $\boldsymbol{y} \in e^{gf}_k$ are expressed through a linear combination of shape functions $\Phi^{e_k}_m(\eta_1, \eta_2)$ weighing the coordinates of the element geometrical vertices $y^{e_k}_{mi}$, while the unknown boundary displacement and traction fields are expressed through a linear combination of shape functions weighing the *nodal* values of boundary displacements $\check{U}^{e_k}_{li}$ and tractions $\check{T}^{e_k}_{li}$, defined with respect to locally defined 2D (surface) coordinate systems $\{\eta_1, \eta_2\}$, so that

$$y_i = \sum_m \Phi^{e_k}_m(\eta_1, \eta_2)\, y^{e_k}_{mi}, \qquad \check{U}_I = \sum_l \Phi^{e_k}_l(\eta_1, \eta_2)\, \check{U}^{e_k}_{lI}, \qquad \check{T}_I = \sum_l \Phi^{e_k}_l(\eta_1, \eta_2)\, \check{T}^{e_k}_{lI} \tag{28}$$

where $i = 1, 2, 3$ and $I = 1, \ldots, 4$ denote the coordinate and generalized components respectively, m spans the geometrical nodes associated with the considered element (either 3 or 4), and l spans the its functional nodes. Considering the above approximation and denoting with $J(\boldsymbol{\eta})$ the Jacobian of the coordinates transformation $y_i = y_i(\eta_1, \eta_2)$, each of the integrals appearing in the integral decomposition in Eq.(27) may be written as

$$\int_{e^{gf}_k} \check{F}^*_{ij}\check{V}_j d\Gamma_y = \left[\int_{e^{gf}_k} \check{F}^*_{ij}(\boldsymbol{x}_n, \boldsymbol{\eta})\, \Phi^{e_k}_l(\boldsymbol{\eta}) J(\boldsymbol{\eta})\, d\eta_1\eta_2\right] \check{V}^{e_k}_{lj}, \tag{29}$$

which can be numerical evaluated using a suitable quadrature rule; in the numerical integration, specific procedures must be employed when the collocation point belongs to the element being integrated, i.e. when $\boldsymbol{x}_n \in e^{gf}_k$, as *singular integrals* arise in such a case. For further discussion about such aspects, interested readers are referred to Refs. [15, 16].

In particular, considering the left-hand side of Eqs.(24), the numerical integration over an element e^{gf}_k yields

$$\fint_{e^{gf}_k} \check{\check{T}}^*_{ij}\check{U}_j d\Gamma_y = \underbrace{\left[\fint_{e^{gf}_k} \check{\check{T}}^*_{ij}(\boldsymbol{x}_n, \boldsymbol{\eta})\, \Phi^{e_k}_l(\boldsymbol{\eta}) J(\boldsymbol{\eta})\, d\eta_1\eta_2\right]}_{\hat{\mathbf{H}} \text{ matrix entries}} \check{U}^{e_k}_{lj} \quad \rightarrow \quad \hat{\mathbf{H}}^{e_k}\check{\mathbf{U}}^{e_k}, \tag{30}$$

and

$$\int_{e^{gf}_k} \check{U}^*_{ij}\check{T}_j d\Gamma_y = \underbrace{\left[\int_{e^{gf}_k} \check{U}^*_{ij}(\boldsymbol{x}_n, \boldsymbol{\eta})\, \Phi^{e_k}_l(\boldsymbol{\eta}) J(\boldsymbol{\eta})\, d\eta_1\eta_2\right]}_{\mathbf{G} \text{ matrix entries}} \check{T}^{e_k}_{lj} \quad \rightarrow \quad \mathbf{G}^{e_k}\check{\mathbf{T}}^{e_k}, \tag{31}$$

where the vectors $\check{\mathbf{U}}^{e_k}$, $\check{\mathbf{T}}^{e_k}$ collect the generalized displacement and traction components associated with the $N_n^{e_k}$ functional nodes belonging to e_k^{gf}, while $\hat{\mathbf{H}}^{e_k}, \mathbf{G}^{e_k} \in \mathbb{R}^{4\times 4N_n^{e_k}}$ are matrix blocks contributing to the population of the larger grain matrices $\hat{\mathbf{H}}^g, \mathbf{G}^g \in \mathbb{R}^{4N_n^g \times 4N_n^g}$, which multiply respectively the vectors $\check{\mathbf{U}}^g$, $\check{\mathbf{T}}^g \in \mathbb{R}^{4N_n^g \times 1}$ collecting the generalized components of displacements and tractions for all the grain functional nodes, N_n^g being the total number of nodes associated with the considered grain g. When collocated at a specific boundary node $\boldsymbol{x}_n$, the integration of Eqs.(24) allows computing four rows of the matrices $\hat{\mathbf{H}}^g$ and $\mathbf{G}^g$: the whole matrices are populated by sequentially collocating them over all the N_n^g nodes associated with the grain in the meshing procedure.

When all the terms in Eqs.(24) are considered, the numerical scheme leads, for each grain, to the system

$$\hat{\mathbf{H}}^g \check{\mathbf{U}}^g - \mathbf{G}^g \check{\mathbf{T}}^g = \left(\mathbf{H}^g \tilde{\mathbf{U}}^g - \mathbf{G}^g \tilde{\mathbf{T}}^g \right) \boldsymbol{\alpha}^g \tag{32}$$

where: the matrix $\mathbf{H}^g \in \mathbb{R}^{4N_n^g \times 4N_n^g}$ is obtained from the integrals involving the kernels $T_{ij}^* \neq \hat{T}_{ij}^*$, and it is then different from $\hat{\mathbf{H}}^g$, although both can be computed simultaneously within the same routine; the terms $\tilde{\mathbf{U}}^g, \tilde{\mathbf{T}}^g \in \mathbb{R}^{4N_n^g \times 4N_s^g}$ are *known* matrices obtained by collocating the particular solutions $\tilde{U}_{jk}^s$ and $\tilde{T}_{jk}^s$ introduced in Section 4.2, and detailed in Appendix B, at the mesh boundary nodes, N_s^g being the number of tensorial terms employed in the series expansion in Eq.(21); eventually $\boldsymbol{\alpha}^g \in \mathbb{R}^{4N_s^g \times 1}$ are the *unknown* coefficients of the mentioned series expansion, to be expressed in terms of the unknown components of displacements for the actual solution of the problem, as it will be discussed in the next section.

5.3. Volume terms approximation coefficients α

In the application of the dual reciprocity method to classical or generalized elastodynamics, for the solution of Eq.(32) the unknown coefficients $\boldsymbol{\alpha}$ appearing in the series expansion given in Eq.(21) – the superscript g is momentarily dropped for the sake of readability – are quite naturally expressed in terms of the time derivatives of the nodal components of displacements $\check{\mathbf{U}}$, see e.g. Refs. [39, 62, 51]. An analogous technique was proposed in Ref.[43] for anisotropic thermo-elasticity, although the functional form of the body terms as spatial derivative of the generalized displacements, see Eq.(18), requires a slightly more involved treatment, briefly recalled below.

First of all, it is observed that, selecting $N_s^g = N_n^g$ and collocating Eq.(21) at N_n^g suitably

selected points $\boldsymbol{y}_n$, e.g. at the N_n^g mesh functional nodes, the following link

$$\mathbf{F} = \tilde{\mathbf{F}}\boldsymbol{\alpha} \tag{33}$$

between the vector $\mathbf{F} \in \mathbb{R}^{4N_n^g \times 1}$, collecting the generalized components of the body volume terms, and the vector $\boldsymbol{\alpha}$ is obtained; $\tilde{\mathbf{F}} \in \mathbb{R}^{4N_n^g \times 4N_s^g}$ is the known matrix generated by direct collation at $\boldsymbol{y}_n$ of the tensorial functions $\tilde{F}_{jk}^s = \tilde{F}_{jk}\left(\boldsymbol{x}_s, \boldsymbol{y}_n\right)$, see Section 4.2 and Appendix B for details.

On the other hand, according to the definition in Eq.(18), the body terms F_I may be expressed in terms of derivatives of the temperature, which is a component of generalized displacements U_I; such displacements may themselves be approximated by a series expansion analogous to that employed in Eq.(21), namely

$$U_I\left(\boldsymbol{y}\right) \approx \sum_{n=1}^{N_s^g} \tilde{F}_{IK}'^s \beta_K^s = \sum_{n=1}^{N_s^g} \tilde{F}_{IK}'\left(\boldsymbol{x}_s, \boldsymbol{y}\right) \beta_K^s \tag{34}$$

where $\tilde{F}_{IK}'^s$, in general different from $\tilde{F}_{IK}^s$ – the prime symbol $'$ is used to mark such difference and it is not related to derivation – are suitable known tensorial radial basis functions, see Appendix B for the specific form assumed in this study, while β_K^s are unknown coefficients of the expansion. Accordingly, the spatial derivatives of U_I may be written as

$$U_{I,j}\left(\boldsymbol{y}\right) \approx \sum_{n=1}^{N_s^g} \tilde{F}_{IK,j}'^s \beta_K^s, \tag{35}$$

which in turn allows expressing F_I as

$$F_I\left(\boldsymbol{y}\right) \approx -\sum_{n=1}^{N_s^g} \tilde{B}_{IK}^s \beta_K^s = -\sum_{n=1}^{N_s^g} \left(\Gamma_{IMl} \tilde{F}_{MK,l}'^s\right) \beta_K^s, \tag{36}$$

with

$$\Gamma_{IMl} = \begin{cases} \gamma_{il}, & I = i = 1,2,3, \quad M = 4 \\ 0 & I = 4, \quad M \neq 4 \end{cases} \tag{37}$$

where γ_{il} are the thermo-elasticity constants appearing in Eqs.(2).

Collocating Eqs.(34) and Eqs.(36) at the $N_s^g = N_n^g$ points $\boldsymbol{y}_n$, following the same procedure as that that led to Eq.(33), yields

$$\check{\mathbf{U}} = \tilde{\mathbf{F}}'\boldsymbol{\beta}, \qquad \mathbf{F} = -\tilde{\mathbf{B}}\boldsymbol{\beta}, \tag{38}$$

which, combined with Eq.(33), allow writing

$$\boldsymbol{\alpha} = -\tilde{\mathbf{F}}^{-1}\tilde{\mathbf{B}}\tilde{\mathbf{F}}'^{-1}\check{\mathbf{U}}, \tag{39}$$

which expresses the sought after link between $\boldsymbol{\alpha}$ and $\check{\mathbf{U}}$. Introducing such expression into Eq.(32) eventually provides

$$\left[\hat{\mathbf{H}} + \left(\mathbf{H}\tilde{\mathbf{U}} - \mathbf{G}\tilde{\mathbf{T}}\right)\tilde{\mathbf{F}}^{-1}\tilde{\mathbf{B}}\tilde{\mathbf{F}}'^{-1}\right]\check{\mathbf{U}} = \mathbf{G}\check{\mathbf{T}}, \tag{40}$$

which may be written more compactly as

$$\mathbf{H}^g_{te}\check{\mathbf{U}}^g = \mathbf{G}^g\check{\mathbf{T}}^g, \tag{41}$$

where the reference to the grain g has been restored and the subscript te expresses the influence of the thermo-elastic coupling through the matrix terms added to $\hat{\mathbf{H}}$ at the left-hand side of Eq.(40).

Eq.(39) has been written by assuming $N^g_s = N^g_n$ and collocating the series expansions in Eqs.(21,35,36) at the N^g_n boundary functional nodes; in some instances however, to improve the method accuracy, it may be useful, or necessary, employing N^g_i additional *internal* points, i.e. located within the grain, to which a consistent number of additional integral equations and functional terms in the series expansions are associated. In this work, the use of boundary nodes only has provided accurate results; however, the developed framework may easily accommodate the use of internal nodes, as done e.g. in Ref.[34] for crystal plasticity analysis or in Ref.[25] for transgranular micro-cracking analysis. The interested readers are referred to Ref.[43] and references therein for further information about the use of internal nodes within the context of the DRM.

5.4. Aggregate system and solution

As seen in the previous sections, the collocation, discretization and numerical integration procedures lead, for each grain/crystal g in the aggregate, to a system of the form of Eq.(41), where the generalized components of displacements and tractions of the functional nodes associated with the grains are collected in the vectors $\check{\mathbf{U}}^g$ and $\check{\mathbf{T}}^g$: in such equations, no consideration has been given so far to either boundary or interface conditions and $\check{\mathbf{U}}^g$, $\check{\mathbf{T}}^g$ collect indeed *all* the nodal components of displacement and traction; however, the enforcement of consistent boundary conditions is necessary for the solution of relevant engineering problems, while intergranular continuity conditions are needed to represent the integrity of the polycrystalline specimen.

The enforcement of boundary conditions involves the reordering and regrouping of the nodal components into unknown values $\check{\mathbf{U}}^g_{un}$, $\check{\mathbf{T}}^g_{un}$ and known values $\check{\mathbf{U}}^g_{kn} = \bar{\mathbf{U}}^g$, $\check{\mathbf{T}}^g_{kn} = \bar{\mathbf{T}}^g$, where the known values are generally associated with functional nodes belonging to grain faces lying on the

external surface Γ_{ext} of the aggregate. Such operation leads, for each grain, to a system of the form

$$\mathbf{A}^g \cdot \mathbf{X}^g = \mathbf{B}^g \cdot \mathbf{Y}^g \tag{42}$$

where $\mathbf{X}^g = \left[\check{\mathbf{U}}^g_{un}; \check{\mathbf{T}}^g_{un}\right]$, $\mathbf{Y}^g = \left[\bar{\mathbf{U}}^g; \bar{\mathbf{T}}^g\right]$ collect *unknown* and *prescribed* values of grain-boundary displacements and tractions respectively, while the matrices $\mathbf{A}^g$ and $\mathbf{B}^g$ collect columns from $\mathbf{H}^g_{te}$ and $\mathbf{G}^g$ associated by the matrix-vector multiplications in Eq.(41) with the above unknown and prescribed degrees of freedom [15, 16]. It is worth noting that the vector $\mathbf{X}^g$ also collects the unknown components of intergranular displacements and tractions.

If the considered aggregate contains N_g grains, thus N_g systems of the form specified in Eq.(42) may be written and collected into a unique aggregate system as

$$\mathbf{A}\mathbf{X} = \begin{bmatrix} \mathbf{A}^1 & \mathbf{0} & \cdots & \mathbf{0} \\ \mathbf{0} & \mathbf{A}^2 & \cdots & \mathbf{0} \\ \vdots & \vdots & \ddots & \vdots \\ \mathbf{0} & \mathbf{0} & \cdots & \mathbf{A}^{N_g} \end{bmatrix} \begin{bmatrix} \mathbf{X}^1 \\ \mathbf{X}^2 \\ \vdots \\ \mathbf{X}^{N_g} \end{bmatrix} = \begin{bmatrix} \mathbf{B}^1 & \mathbf{0} & \cdots & \mathbf{0} \\ \mathbf{0} & \mathbf{B}^2 & \cdots & \mathbf{0} \\ \vdots & \vdots & \ddots & \vdots \\ \mathbf{0} & \mathbf{0} & \cdots & \mathbf{B}^{N_g} \end{bmatrix} \begin{bmatrix} \mathbf{Y}^1 \\ \mathbf{Y}^2 \\ \vdots \\ \mathbf{Y}^{N_g} \end{bmatrix} = \mathbf{B}\mathbf{Y}. \tag{43}$$

The aggregate system in the form given above may directly accommodate *external* kinematic and/or static boundary conditions and it may be straightforwardly generalized to include *periodic* boundary conditions, see e.g. [22, 20]; however, it does not include intergranular conditions yet.

The discrete intergranular conditions are enforced by applying at node-by-node level the conditions specified in Section 4.3 at the continuum level; for this purpose, conformal meshes are generated on the faces of contiguous grains coming into contact, so that the functional nodes belonging to different grains share the same geometrical location on the intergranular interface. Following such procedure, the interface conditions may be enforced by associating to Eq.(43) the following system

$$\mathbf{I}_{\mathrm{IG}}\mathbf{X} = \mathbf{0} \tag{44}$$

where $\mathbf{I}_{\mathrm{IG}}$ is a matrix containing only zeros or ones, suitably placed to enforce the continuity of nodal displacements and the equilibrium of nodal tractions for contiguous intergranular nodes.

The aggregate system, comprised of Eqs.(43-44), can eventually be recast in the compact form

$$\begin{bmatrix} \mathbf{A} \\ \mathbf{I}_{\mathrm{IG}} \end{bmatrix} \cdot \mathbf{X} = \begin{bmatrix} \mathbf{B} \cdot \mathbf{Y} \\ \mathbf{0} \end{bmatrix} \quad \rightarrow \quad \mathbf{M} \cdot \mathbf{X} = \mathbf{Z}\left(\lambda\right), \tag{45}$$

where the coefficient matrix $\mathbf{M}$ is highly sparse and thus requires the use of dedicated solvers for the effective solution of the system; in this work, `PARDISO` (`http://www.pardiso-project.org/`) was selected for such a task. In Eq.(45), the loading vector may depend on a loading factor λ, to allow the possibility of expressing the progressive thermo-elastic loading of the aggregate with quasi-steady boundary conditions, see e.g. Ref.[20] for further details.

Eventually it is worth mentioning that, since Eq.(45) stems from a boundary element procedure, higher computational efficiency could be achieved using Krylov iterative solvers in conjunction with special matrix representations, such as fast multipoles [63] or hierarchical matrices [64, 65, 66, 67].

6. Computational thermo-elastic homogenization of polycrystals

The numerical formulation described in Section 5 can be further developed for applications to computational thermo-elastic homogenization of polycrystalline materials. The goal of homogenization is to infer the properties of a material at a certain scale, at which it is conceived as a continuum, from the knowledge of the morphological and constitutive features of its constituents/phases at a lower scale level [12, 68, 69]. More specifically, the thermo-elastic homogenization of polycrystalline materials can be schematically seen as a procedure to infer the *effective* material macroscopic properties C^E_{ijkl}, κ^E_{ij}, and γ^E_{ij} from the knowledge of the aggregate's morphological features, also in terms of grains and grains size distributions, and of the constants C_{ijkl}, κ_{ij} and γ_{ij} of the different grains/crystals forming the aggregate itself; here the superscript E denotes effective macro-properties as opposed to the analogous properties of the micro-constituents.

Homogenization problems are related to the issue of identifying a material *representative volume element* (RVE), which for polycrystalline materials could be defined as an aggregate containing a number of grains large enough so to exhibit homogenized properties that can be considered representative of the macroscopic continuum material, but whose dimensions are small compared with the scale of the macro-solid, so that the homogenized properties can be reasonably attributed to a continuum point of the macro-solid itself [12]. *Computational* material homogenization can be performed by applying suitable macro-boundary conditions to a RVE, solving the corresponding μ-BVP – μ stands for *micro* – within a selected computational framework and then computing suitable volume-averages of the solved micro-fields over the RVE [13]. More specifically, considering an aggregate with N_g grains, without any *a priori* assumption on its representativity, the thermo-

elastic constitutive relationship between macro-fields may be expressed as

$$\begin{bmatrix} \langle \boldsymbol{\sigma} \rangle \\ \langle \boldsymbol{q} \rangle \end{bmatrix} = \begin{bmatrix} \boldsymbol{C}^A & \mathbf{0} & \boldsymbol{\gamma}^A \\ \mathbf{0} & \boldsymbol{\kappa}^A & \mathbf{0} \end{bmatrix} \begin{bmatrix} +\langle \boldsymbol{\varepsilon} \rangle \\ -\langle \nabla\theta \rangle \\ -\langle \theta \rangle \end{bmatrix} \tag{46}$$

where the Voigt notation has been assumed for the mechanical fields $\boldsymbol{\sigma}$ and $\boldsymbol{\varepsilon}$ and constants $\mathbf{C}$, $\boldsymbol{\gamma}$, and where the generic macro-field $\langle \boldsymbol{f} \rangle$, be it either $\langle \boldsymbol{\sigma} \rangle$, $\langle \boldsymbol{q} \rangle$, $\langle \boldsymbol{\varepsilon} \rangle$, $\langle \nabla\theta \rangle$ or $\langle \theta \rangle$, is defined as the average of the corresponding micro-field $\boldsymbol{f}$ over the volume Ω of the aggregate

$$\langle \boldsymbol{f} \rangle = \frac{1}{\Omega} \int_{\Omega} \boldsymbol{f} \, d\Omega. \tag{47}$$

In Eq.(46), the (6×6) matrix $\boldsymbol{C}^A$, the (3×3) matrix $\boldsymbol{\kappa}^A$ and the (6×1) matrix $\boldsymbol{\gamma}^A$ collect, according to the Voigt convention, the components C^A_{ijkl}, κ^A_{ij}, and γ^A_{ij}, where the superscript A denotes *apparent* material properties: since no assumption has been made on the representativity of the aggregate, in general apparent and effective properties do not coincide; however, as the number of grains included in the aggregate increases, making the aggregate itself more representative, then $C^A_{ijkl} \to C^E_{ijkl}$, $\kappa^A_{ij} \to \kappa^E_{ij}$, and $\gamma^A_{ij} \to \gamma^E_{ij}$.

Eqs.(46-47) provide a practical method for estimating the macroscopic material properties: if suitable macro boundary conditions are enforced on a sufficiently large aggregate, e.g. as independent unitary macro strains, thermal gradients or temperature, the sought after macro properties can be estimated as volume averages of the mechanical stress and thermal flux micro-fields after solving the corresponding μ-BVP. Alternative approaches exploit the *ergodicity assumption* and use both ensemble and volume averages over multiple micro-morphologies *smaller* than a fully representative one, so to obtain an estimate of the effective properties by solving several, but individually less computationally challenging, μ-BVPs [70, 71].

In this work, the thermo-elastic homogenization is performed employing the statistical procedure already adopted for standard and piezoelectric polycrystalline materials in Refs.[18, 20, 27]:

i) A set of N_m morphologies, each containing N_g grains, are generated;

ii) Suitable independent unitary macro-BCs are enforced on each morphology and the corresponding μ-BVPs are solved;

iii) The volume averages $\langle \boldsymbol{\sigma} \rangle$ and $\langle \boldsymbol{q} \rangle$ are computed for each considered independent macro BC and for each morphology, so to obtain an estimate of the apparent properties for each aggregate;

iv) The apparent properties are ensemble-averaged over the N_m considered morphologies.

The procedure is repeated increasing the number N_g of grains contained in the generated morphologies, until convergence of the ensemble-averaged apparent properties is obtained, thus providing a reasonable estimate of the effective ones.

Few remarks about the proposed framework, some of them specific to the thermo-elastic problem, are worthwhile. First, it is worth noting that periodic non-prismatic micro-morphologies are generated in step (*i*) and employed in the subsequent steps. As mentioned in Section 2 and discussed in Ref.[20], such a kind of morphologies enhance the convergence of the homogenization procedure as they allow avoiding possible boundary layer artefacts in the BVP resolved micro-fields, induced by the presence of grains fragments resulting from the cutting operations required for obtaining prismatic morphologies.

In step (*ii*), as suggested by the structure of Eq.(46), a set of 10 linearly independent macro thermo-mechanical BCs must be enforced on each aggregate to infer the apparent properties through volume averages. A natural choice consists in enforcing, independently, three unitary normal macro-strains, three unitary shear macro-strains, three unitary temperature macro-gradients, and a unitary temperature homogeneous macro-variation, which allow sequentially populating the columns of the macro constitutive matrix. In compact matrix notation, the ten independent macro-BCs can be expressed as

$$\begin{bmatrix} +\overline{\langle \boldsymbol{\varepsilon} \rangle}^{k} \\ -\overline{\langle \nabla\theta \rangle}^{k} \\ -\overline{\langle \theta \rangle}^{k} \end{bmatrix} = \mathbf{e}_k \qquad k = 1, \ldots, 10 \tag{48}$$

where the over-bar denotes prescribed values, k identifies the considered macro-BC and $\mathbf{e}_k$ is a (10×1) vector whose components are all zero but the *k-th* one, which has value 1. The macro-BCs corresponding to $k = \{1, 6, 7, 10\}$, enforced on a periodic non-prismatic aggregate, are represented in Fig.(3).

It is important to observe that, in order to infer also the thermo-elastic constants $\boldsymbol{\gamma}^A$, the macro-BCs in Eq.(48) have to be applied as a mix of mechanical *periodic* and thermal *kinematic* relationships. Indeed, upon identifying pairs (m, s) of conjugated *master*/*slave* boundary functional nodes on periodically contiguous couples of grains faces, see e.g. Ref[22], the following mechanical

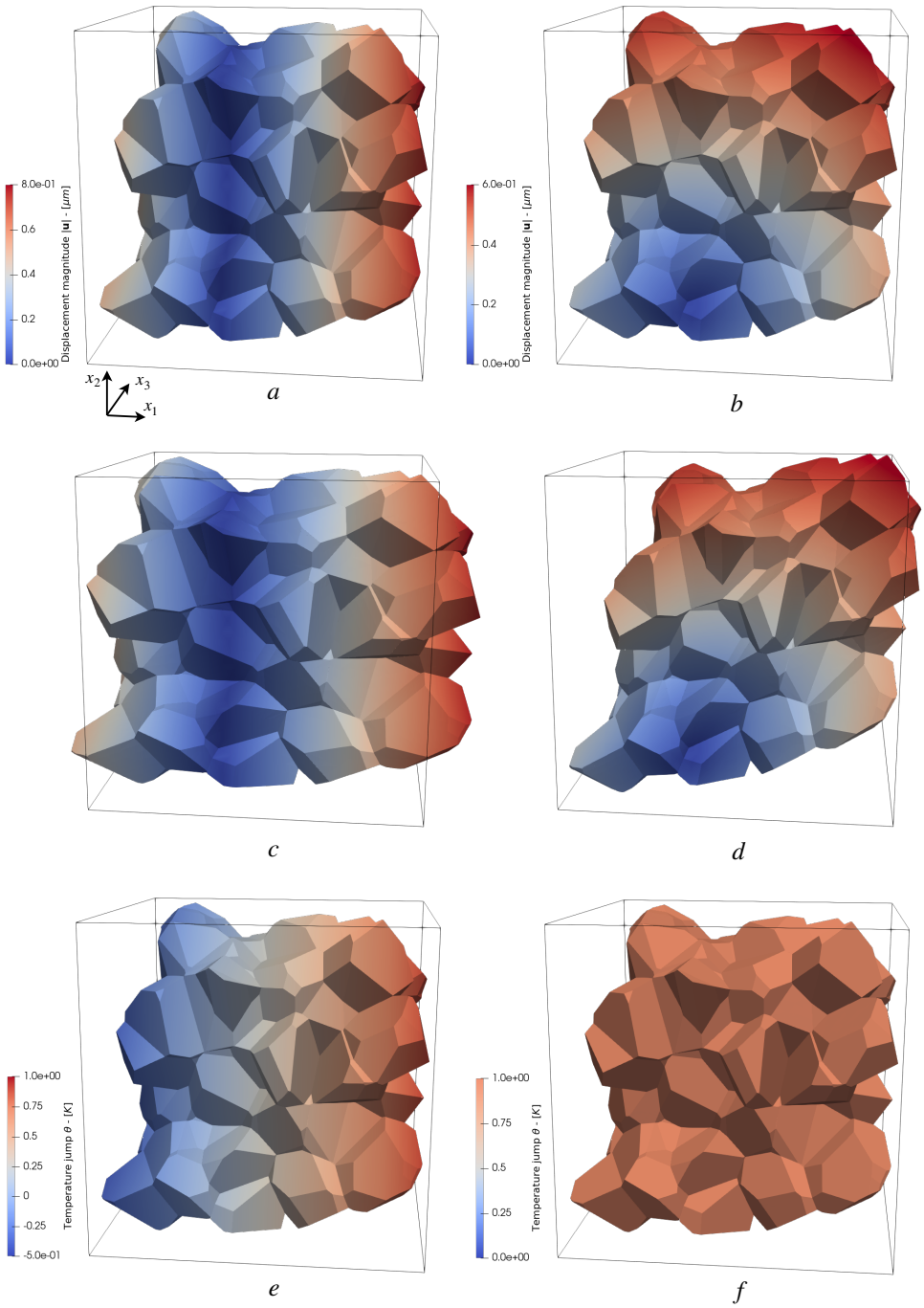

Figure 3: Examples of macro-BCs enforced on the aggregate for the computation of the apparent properties through volume averages: *a*) $\overline{\langle\varepsilon\rangle}_{11} = 1.0$, all the other components in $\{\overline{\langle\boldsymbol{\varepsilon}\rangle}, \overline{\langle\nabla\theta\rangle}, \overline{\langle\theta\rangle}\}$ are null; *b*) $\overline{\langle\varepsilon\rangle}_{12} = \overline{\langle\varepsilon\rangle}_{12} = 0.5$, all the other components are null; *c*) deformed configuration of *a*, amplification factor 0.5; *d*) deformed configuration of *b*, amplification factor 0.5; *e*) $\overline{\langle\nabla\theta\rangle}_1 = 1.0$, all other components null; *f*) $\overline{\langle\theta\rangle} = 1.0$, all other components null. The above BCs would allow the computation of the columns $\{1, 6, 7, 10\}$ of the constitutive matrix in Eq.(46)

periodic boundary conditions (MPBCs)

$$\text{MPBCs} \quad \forall\,(m,s) \quad \begin{cases} \check{u}_i^s + \check{u}_i^m = R_{in}^{sm}\,\overline{\langle\varepsilon\rangle}_{nj}^{k}\left(x_j^s - x_j^m\right) & k = 1,\dots,10 \\ \check{t}_i^s - \check{t}_i^m = 0 & i,j,n = 1,2,3, \end{cases} \tag{49}$$

and the following thermal kinematic boundary conditions (TKBCs)

$$\text{TKBCs} \quad \forall\,(m,s)\,,\forall s \quad \begin{cases} \theta^{fp} = \overline{\langle\theta\rangle}^{k} & \\ \theta^s - \theta^{fp} = \overline{\langle\nabla\theta\rangle}_j^k\left(x_j^s - x_j^{fp}\right) & k = 1,\dots,10 \\ \theta^s - \theta^m = \overline{\langle\nabla\theta\rangle}_j^k\left(x_j^s - x_j^m\right) & j = 1,2,3, \end{cases} \tag{50}$$

are applied, where: the superscript k identifies the applied maco-BCs; the superscripts m and s refer to master and slave nodes respectively; R_{in}^{sm} are the components of the rotation matrix used to express the enforced displacements in the local reference system of the considered periodic interface, over which the (m,s) pair is located; and the superscript *fp* refers to a *fixed point*, to which a specific value of temperature is directly assigned.

Now, while the mechanical relationships in Eqs.(49) represent a set of *periodic* boundary conditions, which enforce *relative* displacements and tractions equilibrium at the periodic interfaces, the thermal relationships in Eqs.(50) have a different nature, as they directly enforce only temperature values on all the external functional nodes of the aggregate: indeed, all temperatures are directly enforced through gradients with respect to the mentioned fixed point, to which the temperature jump $\bar{\theta}$ is directly assigned, while the balance of thermal fluxes is not enforced, leaving its verification as an *a posteriori* assessment. This particular choice allows the possibility of enforcing a homogeneous temperature jump $\overline{\langle\theta\rangle}$ in Eqs.(50), which is needed to estimate the apparent thermo-elastic constants $\boldsymbol{\gamma}^A$ and could not be enforced as a periodic condition.

To better understand the incompatibility between thermal periodic boundary conditions and the application of a homogeneous temperature jump, it should be considered that periodic boundary conditions are generally enforced in terms of gradients, be them strains or temperature gradients: for their numerical application, they thus require that any generalized rigid body modes be removed from the discrete boundary integral equations. Now, a homogeneous temperature jump is precisely a rigid body mode for the thermal problem and its removal would conflict with the application of the TKBCs in Eq.(50), thus preventing the possibility of inferring the thermo-elastic constants $\boldsymbol{\gamma}^A$. Care must thus be taken in ensuring that *only* the mechanical rigid modes are removed. In

this work, such selective removal is achieved recalling that the matrix $\mathbf{H}^g_{te}$ appearing in the grains discrete boundary integral equations – Eq.(41) – has the following structure [43]

$$\mathbf{H}^g_{te} = \begin{bmatrix} \mathbf{H}^g_{uu} & \mathbf{H}^g_{u\theta} \\ \mathbf{0} & \mathbf{H}^g_{\theta\theta} \end{bmatrix}, \tag{51}$$

and applying the technique discussed in Ref.[72] to the matrix block $\mathbf{H}^g_{uu}$, associated with a generic grain, say g (it is sufficient to remove the rigid modes from the integral equations of a single grain).

From the numerical point of view, both the MPBCs and the TKBCs can be applied through the matrix block $\mathbf{I}_{\mathrm{IG}}$ in Eq.(45), which induces a slight modification of the structure of system itself. Indeed, if all the nodal variables related to the external boundary of the aggregate are kept in the vector $\mathbf{X}$ as unknowns, the blocks $\mathbf{B}^g$ do not appear in Eq.(45), and the enforcements of Eqs.(49-50) leads to systems of the form

$$\begin{bmatrix} \mathbf{A} \\ \mathbf{I}_{\mathrm{IG}} \end{bmatrix} \cdot \mathbf{X} = \begin{bmatrix} \mathbf{0} \\ \boldsymbol{\psi}_k \end{bmatrix} \qquad k = 1, \ldots, 10 \tag{52}$$

where k identifies the enforced unitary macro boundary condition. It is interesting to observe that, due to the nature of Eqs.(49-50), the sparsity pattern of the block $\mathbf{I}_{\mathrm{IG}}$ does not change when different macro-BCs are enforced: only the right-hand side of Eq.(52) is affected by the application of the macro-BCs, which allows computing the solution of the ten independent μ-BVPs with a single factorization of the system's coefficient matrix, i.e. with a single call to the `PARDISO` solution routines.

Eventually, it is worth observing that, once the μ-BVP is solved for the considered aggregate, the volume averages of stresses and thermal fluxes, needed for estimating the apparent constitutive properties, may conveniently evaluated as

$$\langle \sigma \rangle_{ij} = \frac{1}{\Omega} \int_\Gamma t_i x_j \, d\Gamma, \qquad \langle q \rangle_i = \frac{1}{\Omega} \int_\Gamma q x_i \, d\Gamma, \tag{53}$$

i.e. through integration, over the external boundary of the morphology, of functions involving mechanical traction components and the thermal normal flux, which are among the primary variables of the proposed formulation and are directly provided by the solution of the μ-BVP.

The procedure for the population of the apparent constitutive matrix in Eq.(46) is schematically depicted in Figs.(4-6)

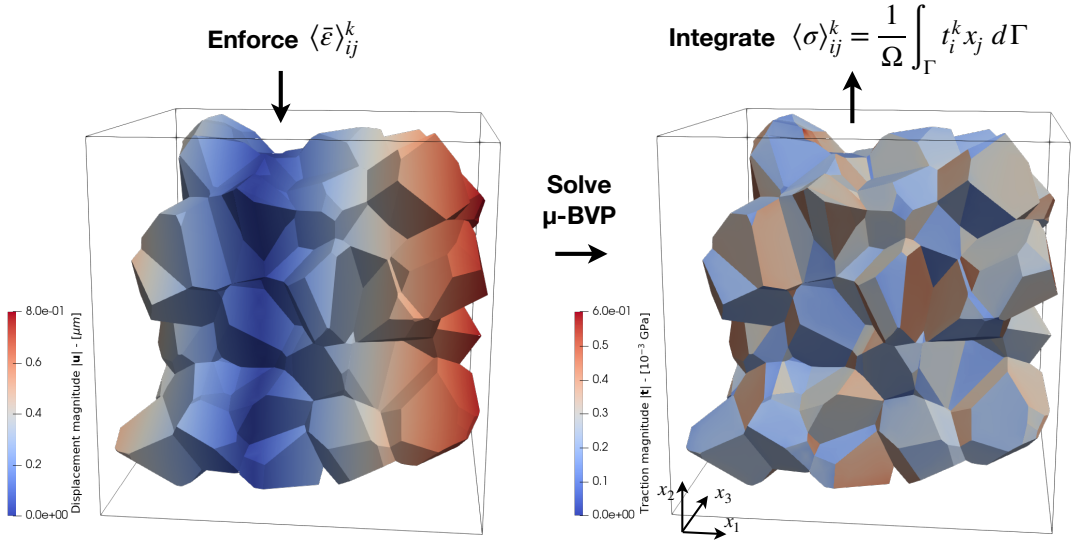

Figure 4: Schematic procedure for the population of the columns $k = \{1, \ldots, 6\}$ of the apparent constitutive matrix in Eq.(46): *i*) suitable mechanical macro-strains $\overline{\langle \boldsymbol{\varepsilon} \rangle}^{k}$ are enforced; *ii*) the μ-BVP is solved with the proposed computational technique and; *iii*) the components of the mechanical tractions are suitably integrated over the surface of the aggregate to compute the related apparent elastic constants.

7. Computational experiments

The statistical computational homogenization approach described in the previous section is applied here to Al_2O_3 and SiC polycrystalline aggregates. Their single-crystal material constants are summarised in Table 1.

For SiC, the elastic coefficients C_{ijkl} are taken from Ref.[73]. The coefficients of thermal expansions $\alpha_{11} = \alpha_{22}$ and α_{33} are retrieved from Refs.[74, 75, 76], which provide for them simple polynomial expressions for temperatures ranging from 0 °C to 1000 °C; the thermo-elastic coefficients γ_{ij} are then computed as $\gamma_{ij} = C_{ijkl}\alpha_{kl}$. The coefficients of thermal conductivity, as computed from first principles, are found in Refs.[77] and confirmed by measurements reported in Ref.[78].

For single-crystal alumina (αAl_2O_3, *corundum*, *sapphire*), the elastic constants at room temperature are given in Ref.[79]. Thermal expansion coefficients are available in Ref.[80] for temperatures ranging between 100 K and 1100 K; the thermal-elastic coefficients can thus be computed from the thermal expansion data, if the stiffness coefficients at that temperature are available. The thermal conductivity coefficients for alumina are taken form Refs.[81, 82]. Other material data for alumina

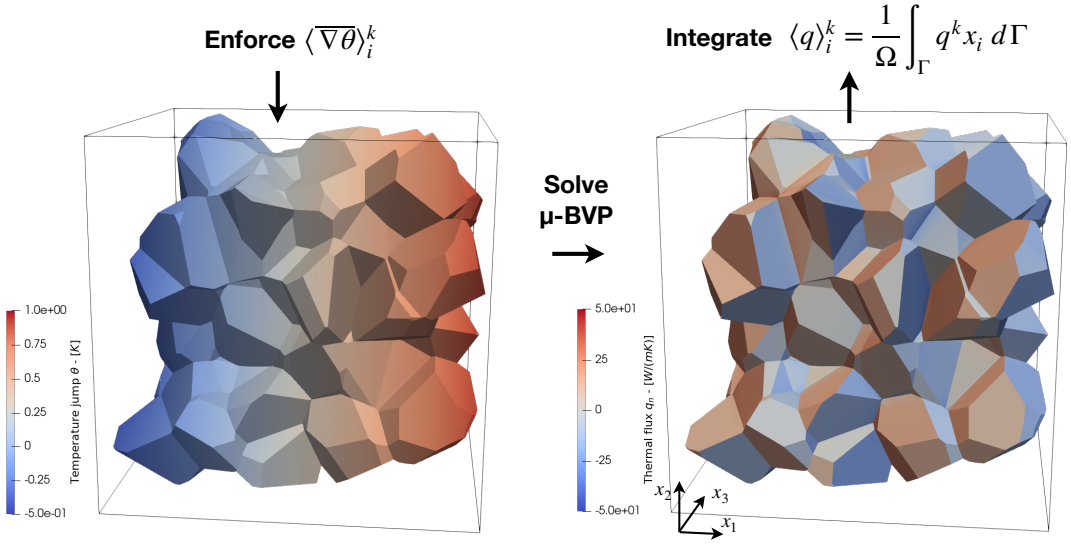

Figure 5: Schematic procedure for the population of the columns $k = \{7, \dots, 9\}$ of the apparent constitutive matrix in Eq.(46): *i*) suitable temperature macro-gradients $\langle \overline{\nabla\theta} \rangle^k$ are enforced; *ii*) the μ-BVP is solved with the proposed computational technique and; *iii*) the thermal normal flux is suitably integrated over the surface of the aggregate to compute the related apparent thermal conductivity constants.

is available in Refs.[83, 84, 85, 86].

The statistical homogenization is implemented considering aggregates with $N_g = \{25, 50, 75, 100\}$ grains, with random orientation in the 3D space assigned to each grain. For each value of N_g, $N_m = 10$ different periodic non-prismatic morphologies are generated, employing `Neper` [45], see Section 2. Each batch of morphologies is employed in the homogenization of both materials. All the generated morphologies are publicly available on *Mendeley Data*[5] through the link provided in the *Data availability* section.

First, the generalized (9×10) matrices of the apparent coefficients, as appearing in Eq.(46) and computed through ensemble averages over $N_m = 10$ morphologies of volume averages on aggregates with $N_g = 100$ grains, here compactly denoted as $\mathbf{K}_{Al_2O_3}^{A(100,10)}$ and $\mathbf{K}_{SiC}^{A(100,10)}$, are reported as directly provided in output by the developed computational framework, to assess the emergence of macroscopic isotropy and exclude the presence of spurious couplings. For polycrystalline alumina,

[5] `https://data.mendeley.com`

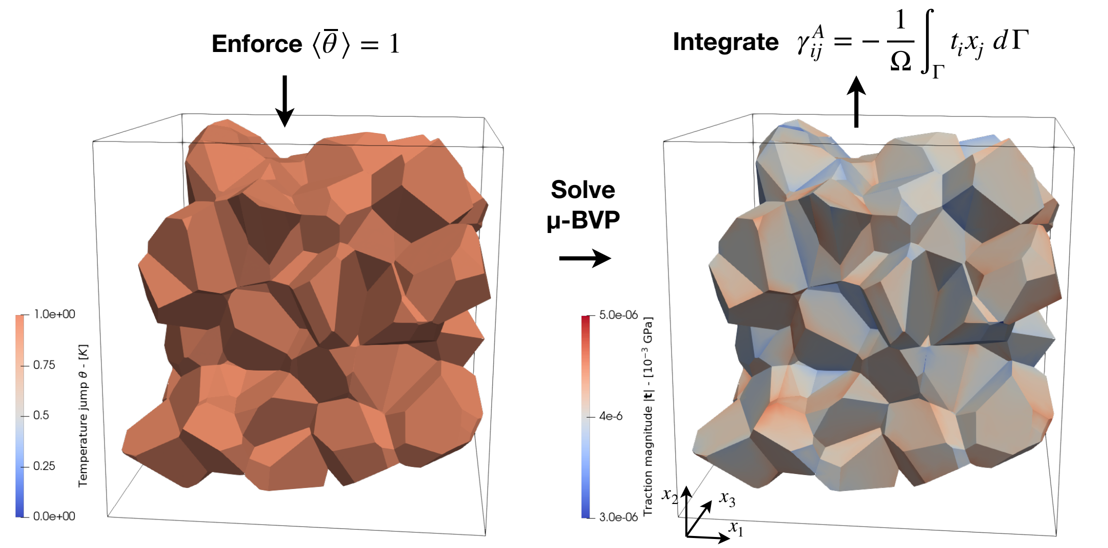

Figure 6: Schematic procedure for the population of the column $k = 10$ of the apparent constitutive matrix in Eq.(46): *i*) a unitary homogeneous temperature macro-variation $\langle\overline{\theta}\rangle$ is enforced; *ii*) the μ-BVP is solved with the proposed computational technique and; *iii*) the components of the mechanical tractions are suitably integrated over the surface of the aggregate to compute the related apparent thermo-elastic constants.

the output for $\mathbf{K}^{A(100,10)}_{Al_2O_3}$ is

$$\left[\begin{array}{cccccc|ccc|c}
\multicolumn{6}{c|}{\overbrace{\hspace{20em}}^{\mathbf{C}}} & & & & \overbrace{}^{\boldsymbol{\gamma}} \\
468.76 & 139.54 & 143.52 & -0.41 & -3.44 & 2.26 & 0.00 & 0.00 & -0.00 & 4.02 \\
139.53 & 470.75 & 141.52 & -0.42 & 0.68 & -0.07 & 0.00 & 0.00 & -0.00 & 4.02 \\
143.52 & 141.49 & 467.94 & 1.36 & 2.51 & -2.02 & 0.00 & 0.00 & -0.00 & 4.04 \\
-0.42 & -0.42 & 1.35 & 163.04 & -2.16 & 0.84 & -0.00 & -0.00 & 0.00 & 0.01 \\
-3.44 & 0.67 & 2.52 & -2.15 & 165.06 & -0.77 & -0.00 & -0.00 & 0.00 & -0.00 \\
2.24 & -0.06 & -2.02 & 0.84 & -0.78 & 161.89 & -0.00 & -0.00 & -0.00 & 0.00 \\
\hline
0.00 & -0.00 & 0.00 & -0.00 & 0.00 & -0.00 & 30.18 & 0.02 & -0.05 & 0.00 \\
0.00 & -0.00 & 0.00 & -0.00 & 0.00 & -0.00 & 0.02 & 30.17 & 0.09 & -0.00 \\
0.00 & -0.00 & 0.00 & -0.00 & 0.00 & -0.00 & -0.05 & 0.08 & 30.38 & 0.00 \\
 & & & & & & \multicolumn{3}{c|}{\underbrace{\hspace{8em}}_{\boldsymbol{\kappa}}} &
\end{array}\right] \tag{54}$$

while for $\mathbf{K}^{A(100,10)}_{SiC}$ it is

Table 1: Material constants for silicon carbide SiC [73, 74, 76, 77, 78] and alumina Al_2O_3 [79, 80, 81]

Material property	Component	SiC	Al_2O_3
Elastic constants	C_{1111}, C_{2222}	502.0	496.8
	C_{3333}	565.0	498.1
	C_{1122}	95.0	163.6
[GPa]	C_{1133}, C_{2233}	96.0	110.9
	C_{1123}, C_{1132}	0.0	-23.5
	C_{2223}, C_{2232}	0.0	23.5
	C_{2323}, C_{1313}	169.0	147.4
	C_{3112}, C_{3121}	0.0	-23.5
	C_{1212}	$(C_{1111} - C_{1122})/2$	
Thermo-elastic constants	γ_{11}, γ_{22}	2.29	4.22
$[10^{-3}\,\mathrm{GPa/K}]$	γ_{33}	2.45	3.67
	γ_{23}, γ_{31}, γ_{12}	0.0	0.0
Thermal conductivity	κ_{11}, κ_{22}	428.8	33.0
$[\mathrm{W/(m \cdot K)}]$	κ_{33}	350.6	25.0

$$
\left[\begin{array}{cccccc|ccc|c}
\multicolumn{6}{c|}{\overbrace{\qquad\qquad\qquad\qquad\qquad\qquad}^{\mathbf{C}}} & & & & \overbrace{\quad}^{\boldsymbol{\gamma}} \\
493.45 & 108.80 & 110.40 & -0.47 & -2.16 & -0.25 & 0.00 & 0.00 & -0.00 & 2.35 \\
108.79 & 496.16 & 107.75 & 2.75 & 0.99 & 0.20 & 0.00 & 0.00 & -0.00 & 2.35 \\
110.40 & 107.75 & 493.05 & -2.94 & 1.50 & -0.13 & 0.00 & 0.00 & -0.00 & 2.35 \\
-0.46 & 2.77 & -2.94 & 191.61 & 0.02 & 0.80 & -0.00 & 0.00 & -0.00 & -0.00 \\
-2.16 & 0.99 & 1.49 & 0.02 & 194.26 & -0.05 & 0.00 & 0.00 & -0.00 & 0.00 \\
-0.26 & 0.20 & -0.13 & 0.79 & -0.05 & 191.77 & 0.00 & 0.00 & -0.00 & -0.00 \\
\hline
0.00 & 0.00 & 0.00 & -0.00 & 0.00 & -0.00 & 390.12 & 0.19 & -0.44 & -0.00 \\
0.00 & 0.00 & 0.00 & -0.00 & 0.00 & -0.00 & 0.20 & 389.99 & 0.86 & -0.00 \\
0.00 & 0.00 & 0.00 & -0.00 & 0.00 & -0.00 & -0.47 & 0.81 & 392.05 & -0.00 \\
 & & & & & & \underbrace{\qquad\qquad\qquad}_{\boldsymbol{\kappa}} & & &
\end{array}\right], \quad (55)
$$

where the units of the different matrix sub-blocks are consistent with those given in Table 1.

For both polycrystalline materials, the main macroscopic symmetries and isotropy are confirmed

in terms of elastic stiffness, thermal conductivity and thermo-elastic coupling, as highlighted by the structure of the sub-blocks $\mathbf{C}^A$, $\boldsymbol{\kappa}^A$ and $\boldsymbol{\gamma}^A$ in Eqs.(54-55). In particular: *i*) the homogenized elastic matrix blocks $\mathbf{C}^A$ exhibit acceptable macroscopic symmetry and do not reveal meaningful coupling between normal and shear components of stress/strain; *ii*) the thermal conductivity blocks $\boldsymbol{\kappa}^A$ tend to become *scalar* matrices, i.e. diagonal matrices with the same value for all the diagonal entries; this is especially true for Al_2O_3, which presents a less pronounced thermal anisotropy at the crystal level with respect to SiC; *iii*) the thermo-elastic constants $\boldsymbol{\gamma}^A$ highlight macroscopic thermo-elastic isotropy and do not reveal the emergence of any spurious thermo-elastic shear stress, i.e. $\gamma_{ij} = 0$ if $i \neq j$. Moreover, correctly, no macroscopic spurious coupling emerges between $\langle \boldsymbol{\sigma} \rangle$ and $\langle \nabla\theta \rangle$ or between $\langle \boldsymbol{q} \rangle$ and $\langle \boldsymbol{\varepsilon} \rangle$ or $\langle \theta \rangle$ in Eq.(46).

Additionally, upon successfully verifying that, for both materials, the coefficients $C_{11}^{A(100,10)}$, $\kappa_{11}^{A(100,10)}$, $\gamma_{11}^{A(100,10)}$ fall within the Reuss' and Voigt's bounds, as done e.g. in Refs.[20, 27]. it has been concluded that both the number of grains $N_g = 100$ considered in the volume averages and the number of morphologies $N_m = 10$ considered in the ensemble averages provide a satisfactory approximation of the effective properties of the considered polycrystals.

Eventually, for giving a better representation of the overall homogenization process, the trends of the volume and ensemble averages vs. N_g are investigated. Fig.(7) shows, for both considered materials, the homogenization results for the stiffness coefficients C_{11}, C_{12} and C_{44}, the thermal conductivity coefficients κ_{ii}, for $i = 1, 2, 3$, and the the thermo-elastic coefficients γ_{ii}, for $i = 1, 2, 3$. In each plot, the black markers + represent the values of the volume averaged property for specific individual aggregates, while the continuous curve represent the ensemble averaged values: the black markers help then provide information about the scattering of the averaged properties that may be expected when considering aggregates containing a certain number of grains N_g. Moreover, in each plot, the shaded area identifies the Reuss' and Voigt's bounds for each considered constant for the two polycrystalline materials.

It can be observed as, in general, the scatter of the specimens' volume averages around the ensemble averages decreases as N_g increases and how both the ensemble averages and almost all the volume averages fall within the Reuss' and Voigt's bounds when $N_g = 100$ for C_{11}, C_{44}, κ_{11}, κ_{22}, γ_{11} and γ_{22}. On the other hand, although the behaviour of the constants C_{12}, κ_{33} and γ_{33} may appear slightly more problematic, this observation does not entail specific concerns, as it might signal the presence of some texture in the considered 100 grains specimens, whose effects could be

removed by considering larger values of N_m and/or N_g, as discussed and shown for example in Refs.[18, 20, 27]. All the data needed to generate Fig.(7) is publicly available on *Mendeley Data*[6] through the link provided in the *Data availability* section.

Eventually, Fig.(8) reports information about system assembly and solution times vs. N_g and about the number of DoFs involved in the proposed computational homogenization procedure. Assembly and solution times refer to the time needed to populate and solve the system in Eq.(52) for an individual morphologies. The averages are computed over the $N_m = 10$ morphologies considered for each value of N_g.

8. Discussion and further developments

In this study, an original multi-region dual reciprocity boundary element framework has been proposed for computational thermo-elastic homogenization of polycrystalline materials. The DRM for single domain anisotropic thermo-elastic analysis had been previously developed by Kögl and Gaul [43]. A multi-region DRM has been proposed by Galvis & Sollero [36] for the analysis of dynamic cracks propagation in 2D polycrystals and by Galvis el al. for dynamic analysis of 3D polycrystals [42]. The present work goes then beyond the state of the art both in terms of methodology, as it extends to multiple regions the technique proposed in Ref.[43] for single regions, and in terms of application, as it considers the problem of polycrystalline thermo-elastic homogenization, not previously covered in the literature with an analogous technique.

At a general level, the developed tool could find application for multiscale analysis of engineering components as well as for the analysis and design of MEMS. In terms of methodology, several directions of further investigation may identified.

First, including a suitable representation of intergranular damage evolution [87, 88, 27, 29, 89], the framework could be extended for the investigation of thermo-mechanic micro-cracking in brittle and quasi-brittle materials, both in a steady-state and transient setting [90, 91]. In this respect, it might be observed that the dependence of the material coefficients on the temperature, i.e. the fact that $C_{ijkl} = C_{ijkl}(T)$, $k_{ij} = k_{ij}(T)$, $\gamma_{ij} = \gamma_{ij}(T)$, has not been accounted for in the formulation, which is suitable for the proposed task of computational homogenization, but could not be an accurate assumption for the analysis of thermal phenomena involving large temperature jumps, e.g.

[6] `https://data.mendeley.com`

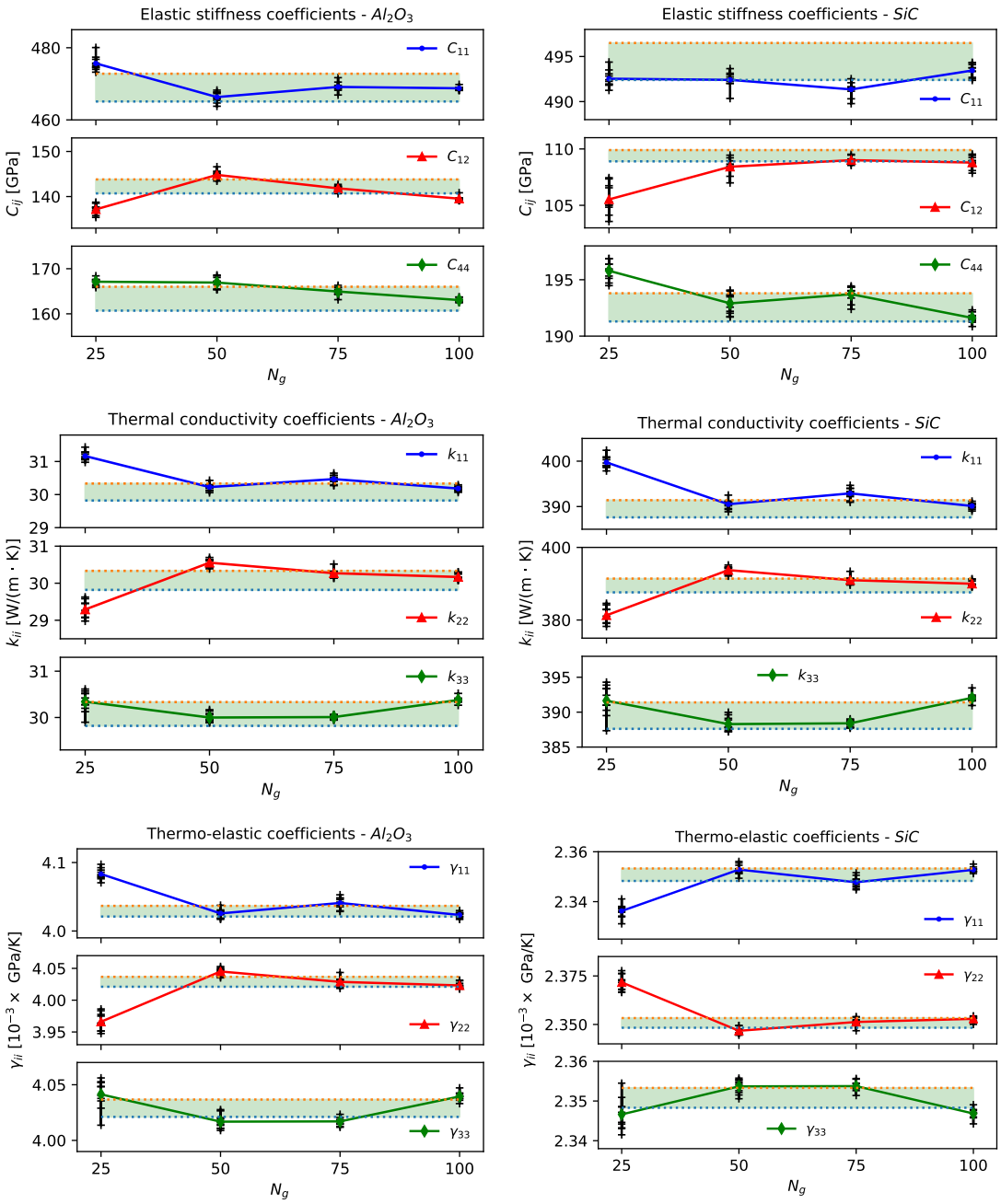

Figure 7: Statistical computational homogenization of selected stiffness coefficients (*top*), thermal conductivity coefficients (*mid-page*), thermo-elastic coefficients (*bottom*) for polycrystalline Al_2O_3 (*left column*) and SiC (*right column*). In each plot the '+' markers represent volume averages for individual specimens, while the continuous curves represent ensemble averages; the shaded area identifies the Reuss' and Voigt's bounds.

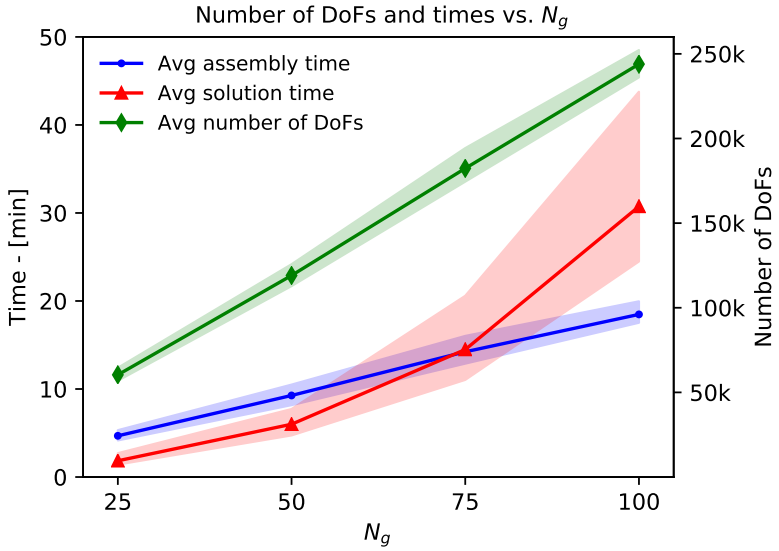

Figure 8: Average system assembly and solution times vs. N_g and number of DoFs vs. N_g for the analysed morphologies. The shaded areas around each curve identify maximum and minimum values. Times and number of DoFs are referred to individual morphologies.

thermal shocks or quenching. A simple method for accounting for such dependency could rely on an iterative implementation with sequential grain-by-grain update of the material coefficients as function of the grain average temperature. More general implementations, for example with point-wise dependency of the material properties on the temperature, would require a deeper reformulation of the boundary integral framework, e.g. drawing from methods developed for the analysis of *functionally graded materials* [92].

Analogously, as the developed numerical/computational DRM architecture can straightforwardly incorporate the representation of inertial terms, the inclusion in the framework of a suitable representation of intergranular de-cohesion under dynamic loading [93, 94] would open to the investigation of dynamic micro-cracking [36] and fragmentation [95] in 3D crystal aggregates. An alternative boundary element framework for polycrystalline elastodynamic analysis could be developed employing a Laplace transform re-formulation of the elastodynamics equations [96, 67], instead of the DRM representation.

For the thermo-elastic analysis of multiphase materials with more complex constitutive behaviours, the present method could by hybridized with other numerical techniques, with the aim

of extending its constitutive modelling capabilities at contained computational cost, in a multi-technique optimization perspective, as proposed for example in Refs.[97, 98], where the boundary element method has been used in conjunction with the rapidly emerging *virtual element method* [99, 100, 101, 102]. In this respect, the hybridization with discontinuous Galerkin methods [103] could offer some definite advantages both in terms of constitutive modelling [104, 105, 106] as well as elastodynamic analysis [107].

Eventually, it is worth observing that, for effective use in multiscale materials modelling, where the solution of many μ-RVEs has to be simultaneous tackled, or for the simulation of larger aggregates, the development of tools with reduced computational costs, both in terms of storage memory and computational time, is generally highly desirable. In this sense, the developed framework is appealing in terms of overall reduction of number of DOFs with respect to other more popular numerical techniques. However, further gains could be obtained employing, for the solution of the thermo-elastic polycrystalline boundary element equations, in either Eq.(45) or Eq.(52), specific iterative solvers in conjunction with special matrix formats, e.g. either fast multipoles [63] or hierarchical matrices [64, 65, 67, 108], which have been proved highly effective in reducing the computational complexity of the solution of systems stemming from boundary integral equations.

9. Conclusions

In this work a three-dimensional framework for thermo-elastic homogenization and analysis of polycrystalline materials has been proposed. The model is built employing from a grain-scale Voronoi representation of crystal aggregates and an integral representation of the thermo-elastic coupling for the individual crystals. Such integral formulation is numerical addressed through a dual reciprocity boundary element method for fully anisotropic thermo-elasticity, which allows to express the overall formulation in terms of intergranular mechanical and thermal variables only, with consequential simplification in terms of data preparation and reduction of the number of degrees of freedom needed for the analysis, with respect to more popular methods. The framework has been tailored and tested for statistical thermo-elastic homogenization of Al_2O_3 and SiC polycrystals. The obtained results have highlighted the effectiveness and robustness of the approach, which may find application in thermo-mechanical multiscale analysis of engineering components.

Data availability

A dataset supporting the finding of this study are openly available on Mendeley Data and can be accessed through the link

https://data.mendeley.com/datasets/m7phkgw3dn/draft?a=4c70825a-0ee6-4dbe-bb8b-76c4539cc17b

The dataset is currently shared for review purposes. It will be published for public open access once the manuscript is accepted for publication.

Acknowledgements

We acknowledge the support of the Italian Ministry of Education, University and Research through the project DEVISU, funded under the scheme PRIN-2107 (Grant 22017ZX9X4K_006). We are grateful to the CINECA's Italian Centre for Super Computing Applications and Innovation staff for granting access to their HPC infrastructure, `http://www.hpc.cineca.it` through the ISCRA Class C project *PolyMats*. We also like to thank Dr. Vincenzo Gulizzi, of the University of Palermo, for useful discussions and comments that helped improve the manuscript.

Appendix A. Anisotropic elastostatic and thermal steady-state Green's functions

As discussed in Section 3.1, the generalized fundamental solutions U^*_{IJ}, T^*_{IJ}, $\hat{T}^*_{IJ}$, defined in Eqs.(13,16) and appearing in Eqs.(17,24), are expressed in terms of the uncoupled elastic and thermal fundamental functions u^*_{ij} and θ^*, defined as the solution of the differential systems in Eqs.(11), and their associated fluxes t^*_{ij}, q^*, given by Eqs.(12), which have to be computed for each grain g of the aggregate.

Following Ref.[109, 110], the elastic kernels $u^*_{ij}(\boldsymbol{x},\boldsymbol{y})$ and their derivatives, and thus also the associated tractions t^*_{ij}, can be computed in terms of spherical harmonics as

$$\frac{\partial^I u^*_{ij}(\boldsymbol{r})}{\partial r_1^{\alpha_1}\partial r_2^{\alpha_2}\partial r_3^{\alpha_3}} = \frac{1}{4\pi r^{I+1}}\sum_{\ell\in\mathcal{L}}^{\infty} P^I_\ell(0)\sum_{m=-\ell}^{\ell}\widetilde{G}^{\ell,m}_{ij,(\alpha_1,\alpha_2,\alpha_3)}Y^m_\ell(\hat{\boldsymbol{r}}), \tag{A.1}$$

where $\boldsymbol{r}\equiv\boldsymbol{y}-\boldsymbol{x}$, $r=\sqrt{r_k r_k}$, $\hat{\boldsymbol{r}}=\boldsymbol{r}/r$; $I=\alpha_1+\alpha_2+\alpha_3$ denotes the order of derivation and $\mathcal{L}$ is the set of positive even (odd) integers when I is even (odd). $P^I_\ell(0)$ is the ℓ-th associated Legendre polynomials of degree I evaluated at 0 and $Y^m_\ell(\hat{\boldsymbol{r}})$ is the spherical harmonic of order ℓ and degree

m. The coefficients $\widetilde{G}^{\ell,m}_{ij,(\alpha_1,\alpha_2,\alpha_3)}$ of the series are computed by means of the following integral over the unit sphere S_1:

$$\widetilde{G}^{\ell,m}_{ij,(\alpha_1,\alpha_2,\alpha_3)} = \int_{S_1} (\hat{\xi}_1)^{\alpha_1}(\hat{\xi}_2)^{\alpha_2}(\hat{\xi}_3)^{\alpha_3}\widetilde{G}_{ij}(\hat{\boldsymbol{\xi}})\bar{Y}^m_\ell(\hat{\boldsymbol{\xi}})\mathrm{d}S(\hat{\boldsymbol{\xi}}), \tag{A.2}$$

being $\widetilde{G}_{ij}(\boldsymbol{\xi}) = [C_{ikjl}\xi_k\xi_l]^{-1}$ and $\bar{Y}^m_\ell$ the complex conjugate of Y^m_ℓ. The interested readers are referred to Ref.[109] for further details.

On the the other hand, following Ref.[43], the thermal kernels θ^*, q^* can be computed as

$$\theta^* = \frac{1}{4\pi J}\frac{1}{r'}, \qquad q^* = \frac{1}{4\pi J}\frac{r_k n_k}{r'^3} \tag{A.3}$$

where $J = \sqrt{\kappa_1\kappa_2\kappa_3}$, κ_i being the *i-th* eigenvalue of the thermal conductivity tensor k_{ij}, and $r' = \sqrt{r_i k^{-1}_{ij} r_j}$, with $r_k = y_k - x_k$.

Appendix B. Particular solutions and matrices for the dual reciprocity method

The particular solutions $\tilde{U}^s_{IJ}$, $\tilde{T}^s_{IJ}$ and $\tilde{F}^s_{IJ}$ employed in the DRM, introduced in Section 4.2, are tensorial radial basis functions associated with a generic source point $\boldsymbol{x}_s$, so that their value at a generic point $\boldsymbol{y}$ may be expressed as

$$\begin{aligned}
\tilde{U}^s_{IJ}(\boldsymbol{y}) &= \tilde{U}_{IJ}(\boldsymbol{x}_s, \boldsymbol{y}) = \tilde{U}_{IJ}(r) \\
\tilde{T}^s_{IJ}(\boldsymbol{y}) &= \tilde{T}_{IJ}(\boldsymbol{x}_s, \boldsymbol{y}) = \tilde{T}_{IJ}(r) \\
\tilde{F}^s_{IJ}(\boldsymbol{y}) &= \tilde{F}_{IJ}(\boldsymbol{x}_s, \boldsymbol{y}) = \tilde{F}_{IJ}(r)
\end{aligned} \tag{B.1}$$

where $I, J = 1, \ldots, 4$ and $r = r(\boldsymbol{x}_s, \boldsymbol{y}) = [(y_k - x_{sk})(y_k - x_{sk})]^{1/2}$, $k = 1, 2, 3$. Using the generalized notation introduced in Section 3.1, they may be written as

$$\tilde{U}^s_{IJ} = \begin{bmatrix} \{\tilde{u}_{ij}\} & \{0\} \\ \{0\} & \tilde{\theta} \end{bmatrix}, \quad \tilde{T}^s_{IJ} = \begin{bmatrix} \{\tilde{t}_{ij}\} & \{0\} \\ \{0\} & \tilde{q} \end{bmatrix}, \quad \tilde{F}^s_{IJ} = \begin{bmatrix} \left\{\tilde{f}_{ij}\right\} & \{0\} \\ \{0\} & -\tilde{\omega} \end{bmatrix} \tag{B.2}$$

where $i, j = 1, 2, 3$. In this work, following Ref.[43], it has been assumed that

$$\tilde{u}_{ij} = \left(r^2 + r^3\right)\delta_{ij}, \qquad \tilde{\theta} = \frac{r^2}{6} + \frac{r^3}{12}, \tag{B.3}$$

from which the following expressions are derived for the elastic tractions and thermal flux fields

$$\begin{aligned}
\tilde{t}_{ij} &= C_{iskl}\,\tilde{u}_{kj,l}\,n_s = C_{iskl}\,(2 + 3r)\,r_l\,\delta_{kj}\,n_s \\
\tilde{q} &= -k_{ij}n_i\tilde{\theta}_{,j} = -k_{ij}n_i r_j\left(\frac{1}{3} + \frac{r}{4}\right)
\end{aligned} \tag{B.4}$$

and for the force and heat source volume density fields

$$\begin{aligned}\tilde{f}_{ij} &= -C_{iskl}\,\tilde{u}_{kj,ls} = -C_{iskl}\left[\frac{3r_l r_s}{r} + (2+3r)\,\delta_{ls}\right]\delta_{kj} \\ \tilde{\omega} &= -k_{ij}\tilde{\theta}_{,ij} = -k_{nn}\left(\frac{1}{3}+\frac{r}{4}\right) - \frac{k_{ij}}{4}\frac{r_i r_j}{r},\end{aligned} \tag{B.5}$$

where $r_k = y_k - x_{sk}$.

On the other hand, the determination of the coefficients $\boldsymbol{\alpha}$ discussed in Section 5.3 requires the definition of the auxiliary functions $\tilde{F}'^{s}_{IJ}$ and their spatial derivatives $\tilde{F}'^{s}_{IJ,k}$, needed to evaluate the functions $\tilde{B}^{s}_{IJ}$, see Eqs.(34-36). In this work, the expressions proposed in Ref.[43] are employed, which read

$$\begin{aligned}\tilde{F}'^{s}_{IJ}(\boldsymbol{y}) &= \tilde{F}'_{IJ}(\boldsymbol{x}_s,\boldsymbol{y}) = \left(1+r^2+r^3\right)\delta_{IJ} \\ \tilde{F}'^{s}_{IJ,k}(\boldsymbol{y}) &= \tilde{F}'_{IJ,k}(\boldsymbol{x}_s,\boldsymbol{y}) = (2+3r)\,r_k\delta_{IJ} \\ \tilde{B}^{s}_{IJ}(\boldsymbol{y}) &= \tilde{B}_{IJ}(\boldsymbol{x}_s,\boldsymbol{y}) = \Gamma_{IMk}\tilde{F}'_{MJ,k}(\boldsymbol{x}_s,\boldsymbol{y}) = \Gamma_{IMk}\,(2+3r)\,r_k\delta_{MJ}\end{aligned} \tag{B.6}$$

with Γ_{IMk} defined as in Eq.(37).

The above definitions allow the straightforward population of the DRM coefficient matrices $\tilde{\mathbf{U}}$, $\tilde{\mathbf{T}}$, $\tilde{\mathbf{F}}$, $\tilde{\mathbf{F}}'$ and $\tilde{\mathbf{B}}$ appearing in Eq.(40). In particular, each of these matrices can be evaluated by direct collocation as

$$\begin{bmatrix} \tilde{\boldsymbol{\Psi}}^{11} & \tilde{\boldsymbol{\Psi}}^{12} & \dots & \tilde{\boldsymbol{\Psi}}^{1N_n^g} \\ \tilde{\boldsymbol{\Psi}}^{21} & \tilde{\boldsymbol{\Psi}}^{22} & \dots & \tilde{\boldsymbol{\Psi}}^{2N_n^g} \\ \vdots & \vdots & \ddots & \vdots \\ \tilde{\boldsymbol{\Psi}}^{N_n^g 1} & \tilde{\boldsymbol{\Psi}}^{N_n^g 2} & \dots & \tilde{\boldsymbol{\Psi}}^{N_n^g N_n^g} \end{bmatrix} \tag{B.7}$$

where the individual matrix blocks $\tilde{\boldsymbol{\Psi}}^{mn} \in \mathbb{R}^{4\times 4}$ are defined by

$$\tilde{\Psi}^{mn}_{IJ} = \begin{cases} \tilde{U}^{mn}_{IJ} = \tilde{U}^{n}_{IJ}(\boldsymbol{x}_m) = \tilde{U}_{IJ}(\boldsymbol{x}_n,\boldsymbol{x}_m) & \rightarrow \quad \tilde{\mathbf{U}} \\ \tilde{T}^{mn}_{IJ} = \tilde{T}^{n}_{IJ}(\boldsymbol{x}_m) = \tilde{T}_{IJ}(\boldsymbol{x}_n,\boldsymbol{x}_m) & \rightarrow \quad \tilde{\mathbf{T}} \\ \tilde{F}^{mn}_{IJ} = \tilde{F}^{n}_{IJ}(\boldsymbol{x}_m) = \tilde{F}_{IJ}(\boldsymbol{x}_n,\boldsymbol{x}_m) & \rightarrow \quad \tilde{\mathbf{F}} \\ \tilde{F}'^{mn}_{IJ} = \tilde{F}'^{n}_{IJ}(\boldsymbol{x}_m) = \tilde{F}'_{IJ}(\boldsymbol{x}_n,\boldsymbol{x}_m) & \rightarrow \quad \tilde{\mathbf{F}}' \\ \tilde{B}^{mn}_{IJ} = \tilde{B}^{n}_{IJ}(\boldsymbol{x}_m) = \tilde{B}_{IJ}(\boldsymbol{x}_n,\boldsymbol{x}_m) & \rightarrow \quad \tilde{\mathbf{B}} \end{cases} \tag{B.8}$$

and can be directly computed from Eqs.(B.1-B.6).

References

[1] J. H. Panchal, S. R. Kalidindi, D. L. McDowell, Key computational modeling issues in integrated computational materials engineering, Computer-Aided Design 45 (1) (2013) 4–25, computer-aided multi-scale materials and product design. doi:https://doi.org/10.1016/j.cad.2012.06.006.
URL https://www.sciencedirect.com/science/article/pii/S0010448512001352

[2] E. B. Tadmor, R. E. Miller, Modeling materials: continuum, atomistic and multiscale techniques, Cambridge University Press, 2011.

[3] W. Ludwig, A. King, P. Reischig, M. Herbig, E. Lauridsen, S. Schmidt, H. Proudhon, S. Forest, P. Cloetens, S. R. du Roscoat, J. BuffiÃĺre, T. Marrow, H. Poulsen, New opportunities for 3d materials science of polycrystalline materials at the micrometre lengthscale by combined use of x-ray diffraction and x-ray imaging, Materials Science and Engineering: A 524 (1) (2009) 69 – 76, special Topic Section: Probing strains and Dislocation Gradients with diffraction. doi:https://doi.org/10.1016/j.msea.2009.04.009.
URL http://www.sciencedirect.com/science/article/pii/S0921509309004511

[4] M. Herbig, A. King, P. Reischig, H. Proudhon, E. M. Lauridsen, J. Marrow, J.-Y. BuffiÃĺre, W. Ludwig, 3-d growth of a short fatigue crack within a polycrystalline microstructure studied using combined diffraction and phase-contrast x-ray tomography, Acta Materialia 59 (2) (2011) 590–601. doi:https://doi.org/10.1016/j.actamat.2010.09.063.
URL https://www.sciencedirect.com/science/article/pii/S1359645410006403

[5] M. F. Pantano, H. D. Espinosa, L. Pagnotta, Mechanical characterization of materials at small length scales, Journal of Mechanical Science and technology 26 (2) (2012) 545–561.

[6] S. Samothrakitis, M. Raventós, J. Čapek, C. B. Larsen, C. Grünzweig, M. Tovar, M. Garcia-Gonzalez, J. Kopeček, S. Schmidt, M. Strobl, Grain morphology reconstruction of crystalline materials from laue three-dimensional neutron diffraction tomography, Scientific Reports 10 (1) (2020) 1–7.

[7] J.-P. Correa-Baena, K. Hippalgaonkar, J. van Duren, S. Jaffer, V. R. Chandrasekhar, V. Stevanovic, C. Wadia, S. Guha, T. Buonassisi, Accelerating materials development via automation, machine learning, and high-performance computing, Joule 2 (8) (2018) 1410–1420.

doi:https://doi.org/10.1016/j.joule.2018.05.009.
URL https://www.sciencedirect.com/science/article/pii/S2542435118302289

[8] R. Lipton, M. Stuebner, Y. Lua, Multi-scale quasistatic damage evolution for polycrystalline materials, International Journal of Engineering Science 58 (2012) 85–94, recent advances in Micromechanics. doi:https://doi.org/10.1016/j.ijengsci.2012.03.027.
URL https://www.sciencedirect.com/science/article/pii/S0020722512000705

[9] P. Chakraborty, Y. Zhang, M. R. Tonks, Multi-scale modeling of microstructure dependent intergranular brittle fracture using a quantitative phase-field based method, Computational Materials Science 113 (2016) 38–52. doi:https://doi.org/10.1016/j.commatsci.2015.11.010.
URL https://www.sciencedirect.com/science/article/pii/S092702561500717X

[10] B. C. Kim, K. Potter, P. M. Weaver, Continuous tow shearing for manufacturing variable angle tow composites, Composites Part A: Applied Science and Manufacturing 43 (8) (2012) 1347–1356. doi:https://doi.org/10.1016/j.compositesa.2012.02.024.
URL https://www.sciencedirect.com/science/article/pii/S1359835X12000929

[11] M. J. Buehler, Materials by design?a perspective from atoms to structures, MRS Bulletin 38 (2) (2013) 169?176. doi:10.1557/mrs.2013.26.

[12] S. Nemat-Nasser, M. Hori, Micromechanics: overall properties of heterogeneous materials, North-Holland series in applied mathematics and mechanics 37.

[13] J. Yvonnet, Computational homogenization of heterogeneous materials with finite elements, Vol. 258, Springer, 2019.

[14] I. Benedetti, F. Barbe, Modelling polycrystalline materials: an overview of three-dimensional grain-scale mechanical models, Journal of Multiscale Modelling 5 (01) (2013) 1350002.

[15] P. Banerjee, The boundary element methods in engineering, McGraw-Hill, 1994, (pp. 177–188).

[16] M. H. Aliabadi, The boundary element method: applications in solids and structures., Vol. 2, John Wiley & Sons Ltd, England, 2002.

[17] G. Sfantos, M. Aliabadi, A boundary cohesive grain element formulation for modelling intergranular microfracture in polycrystalline brittle materials, International journal for numerical methods in engineering 69 (8) (2007) 1590–1626. doi:10.1002/nme.1831.

[18] I. Benedetti, M. Aliabadi, A three-dimensional grain boundary formulation for microstructural modeling of polycrystalline materials, Computational Materials Science 67 (2013) 249 – 260. doi:http://dx.doi.org/10.1016/j.commatsci.2012.08.006.
URL //www.sciencedirect.com/science/article/pii/S0927025612004958

[19] A. F. Galvis, R. Q. RodrÃηguez, P. Sollero, Analysis of three-dimensional hexagonal and cubic polycrystals using the boundary element method, Mechanics of Materials 117 (2018) 58–72. doi:https://doi.org/10.1016/j.mechmat.2017.10.009.
URL https://www.sciencedirect.com/science/article/pii/S016766361730337X

[20] V. Gulizzi, A. Milazzo, I. Benedetti, An enhanced grain-boundary framework for computational homogenization and micro-cracking simulations of polycrystalline materials, Computational Mechanics 56 (4) (2015) 631–651. doi:10.1007/s00466-015-1192-8.

[21] G. Sfantos, M. Aliabadi, Multi-scale boundary element modelling of material degradation and fracture, Computer Methods in Applied Mechanics and Engineering 196 (7) (2007) 1310–1329. doi:10.1016/j.cma.2006.09.004.

[22] I. Benedetti, M. Aliabadi, Multiscale modeling of polycrystalline materials: A boundary element approach to material degradation and fracture, Computer Methods in Applied Mechanics and Engineering 289 (2015) 429 – 453. doi:http://dx.doi.org/10.1016/j.cma.2015.02.018.

[23] J. E. Alvarez, A. F. Galvis, P. Sollero, Multiscale dynamic transition of 2d metallic materials using the boundary element method, Computational Materials Science 155 (2018) 383–392. doi:https://doi.org/10.1016/j.commatsci.2018.09.002.
URL https://www.sciencedirect.com/science/article/pii/S0927025618305962

[24] I. Benedetti, M. Aliabadi, A three-dimensional cohesive-frictional grain-boundary micromechanical model for intergranular degradation and failure in polycrystalline materials, Computer Methods in Applied Mechanics and Engineering 265 (2013) 36–62. doi:10.1016/j.cma.2013.05.023.

[25] V. Gulizzi, C. Rycroft, I. Benedetti, Modelling intergranular and transgranular micro-cracking in polycrystalline materials, Computer Methods in Applied Mechanics and Engineering 329 (2018) 168 – 194. doi:https://doi.org/10.1016/j.cma.2017.10.005.
URL http://www.sciencedirect.com/science/article/pii/S0045782517306746

[26] F. Barbe, I. Benedetti, V. Gulizzi, M. Calvat, C. Keller, Elucidating the effect of bimodal grain size distribution on plasticity and fracture behavior of polycrystalline materials, Journal of Multiscale Modelling 11 (04) (2020) 2050007. arXiv:https://doi.org/10.1142/S1756973720500079, doi:10.1142/S1756973720500079.
URL https://doi.org/10.1142/S1756973720500079

[27] I. Benedetti, V. Gulizzi, A. Milazzo, A microstructural model for homogenisation and cracking of piezoelectric polycrystals, Computer Methods in Applied Mechanics and Engineering 357 (2019) 112595. doi:https://doi.org/10.1016/j.cma.2019.112595.
URL http://www.sciencedirect.com/science/article/pii/S0045782519304712

[28] I. Benedetti, V. Gulizzi, A grain-scale model for high-cycle fatigue degradation in polycrystalline materials, International Journal of Fatigue 116 (2018) 90 – 105. doi:https://doi.org/10.1016/j.ijfatigue.2018.06.010.
URL http://www.sciencedirect.com/science/article/pii/S0142112318302287

[29] F. Parrinello, V. Gulizzi, I. Benedetti, A computational framework for low-cycle fatigue in polycrystalline materials, Computer Methods in Applied Mechanics and Engineering 383 (2021) 113898. doi:https://doi.org/10.1016/j.cma.2021.113898.
URL https://www.sciencedirect.com/science/article/pii/S0045782521002358

[30] I. Benedetti, V. Gulizzi, A. Milazzo, Grain-boundary modelling of hydrogen assisted intergranular stress corrosion cracking, Mechanics of Materials 117 (2018) 137–151. doi:10.1016/j.mechmat.2017.11.001.
URL https://www.scopus.com/inward/record.uri?eid=2-s2.0-85037155275&doi=10.1016%2fj.mechmat.2017.11.001&partnerID=40&md5=38ef17b25776893b9871f8378ae3d731

[31] G. Voronoï, Nouvelles applications des paramètres continus à la théorie des formes quadra-

tiques. deuxième mémoire. recherches sur les paralléllοèdres primitifs., Journal für die reine und angewandte Mathematik 134 (1908) 198–287.

[32] Z. Fan, Y. Wu, X. Zhao, Y. Lu, Simulation of polycrystalline structure with voronoi diagram in laguerre geometry based on random closed packing of spheres, Computational materials science 29 (3) (2004) 301–308.

[33] R. Quey, L. Renversade, Optimal polyhedral description of 3d polycrystals: Method and application to statistical and synchrotron x-ray diffraction data, Computer Methods in Applied Mechanics and Engineering 330 (Supplement C) (2018) 308 – 333. doi:https://doi.org/10.1016/j.cma.2017.10.029.
URL http://www.sciencedirect.com/science/article/pii/S0045782517307028

[34] I. Benedetti, V. Gulizzi, V. Mallardo, A grain boundary formulation for crystal plasticity, International Journal of Plasticity 83 (2016) 202 – 224. doi:http://dx.doi.org/10.1016/j.ijplas.2016.04.010.
URL //www.sciencedirect.com/science/article/pii/S0749641916300596

[35] I. Benedetti, V. Gulizzi, V. Mallardo, Boundary element crystal plasticity method, Journal of Multiscale Modelling 08 (03n04) (2017) 1740003. arXiv:https://doi.org/10.1142/S1756973717400030, doi:10.1142/S1756973717400030.
URL https://doi.org/10.1142/S1756973717400030

[36] A. Galvis, P. Sollero, 2d analysis of intergranular dynamic crack propagation in polycrystalline materials a multiscale cohesive zone model and dual reciprocity boundary elements, Computers & Structures 164 (2016) 1 – 14. doi:https://doi.org/10.1016/j.compstruc.2015.11.004.
URL http://www.sciencedirect.com/science/article/pii/S0045794915003016

[37] G. Geraci, M. H. Aliabadi, Micromechanical modeling of cohesive thermoelastic steady-state and transient cracking in polycrystalline materials, International Journal for Numerical Methods in Engineering 117 (12) (2019) 1205–1233. arXiv:https://onlinelibrary.wiley.com/doi/pdf/10.1002/nme.5997, doi:10.1002/nme.5997.
URL https://onlinelibrary.wiley.com/doi/abs/10.1002/nme.5997

[38] G. Geraci, M. Aliabadi, Micromechanical modelling of cohesive thermoelastic cracking in orthotropic polycrystalline materials, Computer Methods in Applied Mechanics and Engineering 339 (2018) 567–590. doi:https://doi.org/10.1016/j.cma.2018.05.011.
URL https://www.sciencedirect.com/science/article/pii/S0045782518302548

[39] D. Nardini, C. Brebbia, A new approach to free vibration analysis using boundary elements, Applied Mathematical Modelling 7 (3) (1983) 157–162. doi:https://doi.org/10.1016/0307-904X(83)90003-3.
URL https://www.sciencedirect.com/science/article/pii/0307904X83900033

[40] L. Wrobel, C. Brebbia, The dual reciprocity boundary element formulation for nonlinear diffusion problems, Computer Methods in Applied Mechanics and Engineering 65 (2) (1987) 147–164. doi:https://doi.org/10.1016/0045-7825(87)90010-7.
URL https://www.sciencedirect.com/science/article/pii/0045782587900107

[41] L. C. W. P. W. Partridge, C. A. Brebbia, Dual Reciprocity Boundary Element Method, 1st Edition, International Series on Computational Engineering, Springer Science & Business Media, 1991. doi:https://doi.org/10.1007/978-94-011-3690-7.

[42] A. F. Galvis, R. Q. Rodríguez, P. Sollero, Dynamic analysis of three-dimensional polycrystalline materials using the boundary element method, Computers & Structures 200 (2018) 11–20. doi:https://doi.org/10.1016/j.compstruc.2018.02.009.
URL https://www.sciencedirect.com/science/article/pii/S0045794917312774

[43] M. Kögl, L. Gaul, A boundary element method for anisotropic coupled thermoelasticity, Archive of Applied Mechanics 73 (5) (2003) 377–398.

[44] I. Simonovski, L. Cizelj, Towards modeling intergranular stress corrosion cracks on grain size scales, Nuclear Engineering and Design 246 (0) (2012) 107–114.

[45] R. Quey, P. R. Dawson, F. Barbe, Large scale 3D random polycrystals for the finite element method: Generation, meshing and remeshing, Computer Methods in Applied Mechanics and Engineering 200 (2011) 1729–1745.

[46] A. Lyckegaard, E. M. Lauridsen, W. Ludwig, R. W. Fonda, H. F. Poulsen, On the use of laguerre tessellations for representations of 3d grain structures, Advanced Engineering

Materials 13 (3) (2011) 165–170. doi:10.1002/adem.201000258.
URL http://dx.doi.org/10.1002/adem.201000258

[47] C. H. Rycroft, Voro++: A three-dimensional Voronoi cell library in C++, Chaos 19 (2009) 041111.

[48] P. H. Serrao, S. Sandfeld, A. Prakash, Optimic: A tool to generate optimized polycrystalline microstructures for materials simulations, SoftwareX 15 (2021) 100708. doi:https://doi.org/10.1016/j.softx.2021.100708.
URL https://www.sciencedirect.com/science/article/pii/S2352711021000534

[49] A. Abdelkader, C. L. Bajaj, M. S. Ebeida, A. H. Mahmoud, S. A. Mitchell, J. D. Owens, A. A. Rushdi, Vorocrust: Voronoi meshing without clipping, ACM Trans. Graph. 39 (3). doi:10.1145/3337680.
URL https://doi.org/10.1145/3337680

[50] J. Bomidi, N. Weinzapfel, F. Sadeghi, Three-dimensional modelling of intergranular fatigue failure of fine grain polycrystalline metallic mems devices, Fatigue & Fracture of Engineering Materials & Structures 35 (11) (2012) 1007–1021.

[51] M. Kögl, L. Gaul, A boundary element method for transient piezoelectric analysis, Engineering Analysis with Boundary Elements 24 (7) (2000) 591–598. doi:https://doi.org/10.1016/S0955-7997(00)00039-4.
URL https://www.sciencedirect.com/science/article/pii/S0955799700000394

[52] F. Rizzo, D. Shippy, An advanced boundary integral equation method for three-dimensional thermoelasticity, International Journal for Numerical Methods in Engineering 11 (11) (1977) 1753–1768.

[53] V. Sládek, J. Sládek, Boundary integral equation method in thermoelasticity part i: general analysis, Applied Mathematical Modelling 7 (4) (1983) 241–253. doi:https://doi.org/10.1016/0307-904X(83)90077-X.
URL https://www.sciencedirect.com/science/article/pii/0307904X8390077X

[54] V. Sládek, J. Sládek, Boundary integral equation method in thermoelasticity part iii: uncoupled thermoelasticity, Applied Mathematical Modelling 8 (6) (1984) 413–418. doi:https:

//doi.org/10.1016/0307-904X(84)90047-7.
URL https://www.sciencedirect.com/science/article/pii/0307904X84900477

[55] V. Sládek, J. Sládek, A new approach to transient dynamic analysis of thermoelasticity by the boundary element method, Engineering Analysis 2 (4) (1985) 221–229. doi:https://doi.org/10.1016/0264-682X(85)90036-X.
URL https://www.sciencedirect.com/science/article/pii/0264682X8590036X

[56] G. Dargush, P. Banerjee, Boundary element methods in three-dimensional thermoelasticity, International Journal of Solids and Structures 26 (2) (1990) 199–216. doi:https://doi.org/10.1016/0020-7683(90)90052-W.
URL https://www.sciencedirect.com/science/article/pii/002076839090052W

[57] D. Dell'Erba, M. Aliabadi, D. Rooke, Dual boundary element method for three-dimensional thermoelastic crack problems, International journal of fracture 94 (1) (1998) 89–101.

[58] M. Hematiyan, M. Mohammadi, L. Marin, A. Khosravifard, Boundary element analysis of uncoupled transient thermo-elastic problems with time- and space-dependent heat sources, Applied Mathematics and Computation 218 (5) (2011) 1862–1882. doi:https://doi.org/10.1016/j.amc.2011.06.070.
URL https://www.sciencedirect.com/science/article/pii/S0096300311009155

[59] Y. Shiah, C. Tan, Boundary element method for thermoelastic analysis of three-dimensional transversely isotropic solids, International Journal of Solids and Structures 49 (21) (2012) 2924–2933. doi:https://doi.org/10.1016/j.ijsolstr.2012.05.025.
URL https://www.sciencedirect.com/science/article/pii/S0020768312002351

[60] L. C. Wrobel, The boundary element method, volume 1: Applications in thermo-fluids and acoustics, Vol. 1, John Wiley & Sons, 2002.

[61] Q. Deng, C. G. Li, S. L. Wang, H. Tang, H. Zheng, A new method to the treatment of corners in the bem, Engineering Analysis with Boundary Elements 37 (1) (2013) 182 – 186. doi:https://doi.org/10.1016/j.enganabound.2012.03.017.
URL http://www.sciencedirect.com/science/article/pii/S0955799712001439

[62] L. G. M. Kögl, A 3-d boundary element method for dynamic analysis of anisotropic elastic solids, Computer Modeling in Engineering & Sciences 1 (4) (2000) 27–44.
URL http://www.techscience.com/CMES/v1n4/24706

[63] Y. Liu, Fast multipole boundary element method: theory and applications in engineering, Cambridge university press, 2009.

[64] M. Bebendorf, Hierarchical matrices: a means to efficiently solve elliptic boundary value problems, Vol. 63, Springer Science & Business Media, 2008.

[65] I. Benedetti, M. Aliabadi, G. Davì, A fast 3d dual boundary element method based on hierarchical matrices, International Journal of Solids and Structures 45 (7) (2008) 2355 – 2376. doi:http://dx.doi.org/10.1016/j.ijsolstr.2007.11.018.
URL //www.sciencedirect.com/science/article/pii/S0020768307005008

[66] I. Benedetti, A. Milazzo, M. H. Aliabadi, A fast dual boundary element method for 3d anisotropic crack problems, International Journal for Numerical Methods in Engineering 80 (10) (2009) 1356–1378. doi:10.1002/nme.2666.
URL http://dx.doi.org/10.1002/nme.2666

[67] I. Benedetti, M. H. Aliabadi, A fast hierarchical dual boundary element method for three-dimensional elastodynamic crack problems, International Journal for Numerical Methods in Engineering 84 (9) (2010) 1038–1067. doi:10.1002/nme.2929.
URL http://dx.doi.org/10.1002/nme.2929

[68] I. Benedetti, H. Nguyen, R. A. Soler-Crespo, W. Gao, L. Mao, A. Ghasemi, J. Wen, S. Nguyen, H. D. Espinosa, Formulation and validation of a reduced order model of 2d materials exhibiting a two-phase microstructure as applied to graphene oxide, Journal of the Mechanics and Physics of Solids 112 (2018) 66–88. doi:https://doi.org/10.1016/j.jmps.2017.11.012.
URL https://www.sciencedirect.com/science/article/pii/S002250961730892X

[69] W. Guo, F. Han, J. Jiang, W. Xu, A micromechanical framework for thermo-elastic properties of multiphase cementitious composites with different saturation degrees, International Journal of Mechanical Sciences (2022) 107313doi:https://doi.org/10.1016/j.ijmecsci.2022.107313.
URL https://www.sciencedirect.com/science/article/pii/S0020740322002260

[70] T. Kanit, S. Forest, I. Galliet, V. Mounoury, D. Jeulin, Determination of the size of the representative volume element for random composites: statistical and numerical approach, International Journal of Solids and Structures 40 (13) (2003) 3647–3679. doi:https://doi.org/10.1016/S0020-7683(03)00143-4.
URL https://www.sciencedirect.com/science/article/pii/S0020768303001434

[71] D. Jeulin, T. Kanit, S. Forest, Representative volume element: A statistical point of view, in: D. J. Bergman, E. Inan (Eds.), Continuum Models and Discrete Systems, Springer Netherlands, Dordrecht, 2004, pp. 21–27.

[72] E. Lutz, W. Ye, S. Mukherjee, Elimination of rigid body modes from discretized boundary integral equations, International Journal of Solids and Structures 35 (33) (1998) 4427–4436. doi:https://doi.org/10.1016/S0020-7683(97)00261-8.
URL https://www.sciencedirect.com/science/article/pii/S0020768397002618

[73] G. Arlt, G. R. Schodder, Some elastic constants of silicon carbide, The Journal of the Acoustical Society of America 37 (2) (1965) 384–386. arXiv:https://doi.org/10.1121/1.1909336, doi:10.1121/1.1909336.
URL https://doi.org/10.1121/1.1909336

[74] Z. Li, R. Bradt, Thermal expansion of the hexagonal (6h) polytype of silicon carbide, Journal of the American Ceramic Society 69 (12) (1986) 863–866.

[75] Z. Li, R. C. Bradt, Thermal expansion of the hexagonal (4h) polytype of sic, Journal of Applied Physics 60 (2) (1986) 612–614. arXiv:https://doi.org/10.1063/1.337456, doi:10.1063/1.337456.
URL https://doi.org/10.1063/1.337456

[76] Z. Li, R. Bradt, Thermal expansion and thermal expansion anisotropy of sic polytypes, Journal of the American Ceramic Society 70 (7) (1987) 445–448.

[77] N. H. Protik, A. Katre, L. Lindsay, J. Carrete, N. Mingo, D. Broido, Phonon thermal transport in 2h, 4h and 6h silicon carbide from first principles, Materials Today Physics 1 (2017) 31–38. doi:https://doi.org/10.1016/j.mtphys.2017.05.004.
URL https://www.sciencedirect.com/science/article/pii/S2542529317300743

[78] X. Qian, P. Jiang, R. Yang, Anisotropic thermal conductivity of 4h and 6h silicon carbide measured using time-domain thermoreflectance, Materials Today Physics 3 (2017) 70–75. doi:https://doi.org/10.1016/j.mtphys.2017.12.005.
URL https://www.sciencedirect.com/science/article/pii/S2542529317302262

[79] J. Wachtman Jr, W. Tefft, D. Lam Jr, R. Stinchfield, Elastic constants of synthetic single crystal corundum at room temperature, Journal of Research of the National Bureau of Standards. Section A, Physics and Chemistry 64 (3) (1960) 213.

[80] J. B. Wachtman JR., T. G. Scuderi, G. W. Cleek, Linear thermal expansion of aluminum oxide and thorium oxide from 100 to 1100k, Journal of the American Ceramic Society 45 (7) (1962) 319–323. arXiv:https://ceramics.onlinelibrary.wiley.com/doi/pdf/10.1111/j.1151-2916.1962.tb11159.x, doi:https://doi.org/10.1111/j.1151-2916.1962.tb11159.x.
URL https://ceramics.onlinelibrary.wiley.com/doi/abs/10.1111/j.1151-2916.1962.tb11159.x

[81] R. Monchamp, Preparation and properties of crystalline laser oxide materials, Journal of Solid State Chemistry 12 (3) (1975) 201–206. doi:https://doi.org/10.1016/0022-4596(75)90306-0.
URL https://www.sciencedirect.com/science/article/pii/0022459675903060

[82] D. Rodin, S. K. Yee, Simultaneous measurement of in-plane and through-plane thermal conductivity using beam-offset frequency domain thermoreflectance, Review of Scientific Instruments 88 (1) (2017) 014902. arXiv:https://doi.org/10.1063/1.4973297, doi:10.1063/1.4973297.
URL https://doi.org/10.1063/1.4973297

[83] F. Charvat, W. Kingery, Thermal conductivity: xiii, effect of microstructure on conductivity of single-phase ceramics, Journal of the american ceramic society 40 (9) (1957) 306–315.

[84] G. A. Slack, Thermal conductivity of mgo, al_2o_3, $mgal_2o_4$, and fe_3o_4 crystals from 3° to 300°k, Phys. Rev. 126 (1962) 427–441. doi:10.1103/PhysRev.126.427.
URL https://link.aps.org/doi/10.1103/PhysRev.126.427

[85] A. M. Hofmeister, Thermal diffusivity and thermal conductivity of single-crystal mgo and al2o3 and related compounds as a function of temperature, Physics and Chemistry of Minerals 41 (5) (2014) 361–371.

[86] X. Wu, L. Tang, C. L. Hardin, C. Dames, Y. Kodera, J. E. Garay, Thermal conductivity and management in laser gain materials: A nano/microstructural perspective, Journal of Applied Physics 131 (2) (2022) 020902. arXiv:https://doi.org/10.1063/5.0073507, doi:10.1063/5.0073507.
URL https://doi.org/10.1063/5.0073507

[87] A. Hattiangadi, T. Siegmund, A numerical study on interface crack growth under heat flux loading, International Journal of Solids and Structures 42 (24) (2005) 6335–6355. doi:https://doi.org/10.1016/j.ijsolstr.2005.05.050.
URL https://www.sciencedirect.com/science/article/pii/S0020768305002994

[88] A. Sapora, M. Paggi, A coupled cohesive zone model for transient analysis of thermoelastic interface debonding, Computational Mechanics 53 (4) (2014) 845–857.

[89] F. Parrinello, I. Benedetti, A coupled plasticity-damage cohesive-frictional interface for low-cycle fatigue analysis, International Journal of Mechanical Sciences 224 (2022) 107298. doi:https://doi.org/10.1016/j.ijmecsci.2022.107298.
URL https://www.sciencedirect.com/science/article/pii/S0020740322002132

[90] G. Geraci, M. Aliabadi, Micromechanical boundary element modelling of transgranular and intergranular cohesive cracking in polycrystalline materials, Engineering Fracture Mechanics 176 (2017) 351–374.

[91] T. Wang, H. Han, Y. Wang, X. Ye, G. Huang, Z. Liu, Z. Zhuang, Simulation of crack patterns in quasi-brittle materials under thermal shock using phase field and cohesive zone models, Engineering Fracture Mechanics 276 (2022) 108889. doi:https://doi.org/10.1016/j.engfracmech.2022.108889.
URL https://www.sciencedirect.com/science/article/pii/S0013794422006075

[92] A. Sutradhar, G. H. Paulino, The simple boundary element method for transient heat conduction in functionally graded materials, Computer Methods in Applied Mechanics and En-

gineering 193 (42) (2004) 4511–4539. doi:https://doi.org/10.1016/j.cma.2004.02.018.
URL https://www.sciencedirect.com/science/article/pii/S0045782504001847

[93] J. Huang, C. Zhang, J. Wang, C. Zhang, On the applicability of rate-dependent cohesive zone models in low-velocity impact simulation, Engineering Fracture Mechanics 271 (2022) 108659. doi:https://doi.org/10.1016/j.engfracmech.2022.108659.
URL https://www.sciencedirect.com/science/article/pii/S001379442200385X

[94] T. Gu, Z. Wang, A strain rate-dependent cohesive zone model for shear failure of hat-shaped specimens under impact, Engineering Fracture Mechanics 259 (2022) 108145. doi:https://doi.org/10.1016/j.engfracmech.2021.108145.
URL https://www.sciencedirect.com/science/article/pii/S0013794421005506

[95] B. Ren, S. Li, A three-dimensional atomistic-based process zone model simulation of fragmentation in polycrystalline solids, International Journal for Numerical Methods in Engineering 93 (9) (2013) 989–1014. arXiv:https://onlinelibrary.wiley.com/doi/pdf/10.1002/nme.4430, doi:https://doi.org/10.1002/nme.4430.
URL https://onlinelibrary.wiley.com/doi/abs/10.1002/nme.4430

[96] P. Wen, M. Aliabadi, D. Rooke, Cracks in three dimensions: A dynamic dual boundary element analysis, Computer Methods in Applied Mechanics and Engineering 167 (1) (1998) 139–151. doi:https://doi.org/10.1016/S0045-7825(98)00116-9.
URL https://www.sciencedirect.com/science/article/pii/S0045782598001169

[97] M. Lo Cascio, A. Milazzo, I. Benedetti, A hybrid virtual-boundary element formulation for heterogeneous materials, International Journal of Mechanical Sciences 199 (2021) 106404. doi:https://doi.org/10.1016/j.ijmecsci.2021.106404.
URL https://www.sciencedirect.com/science/article/pii/S0020740321001399

[98] M. Lo Cascio, I. Benedetti, Coupling bem and vem for the analysis of composite materials with damage, Journal of Multiscale Modelling 13 (01) (2022) 2144001. arXiv:https://doi.org/10.1142/S1756973721440017, doi:10.1142/S1756973721440017.
URL https://doi.org/10.1142/S1756973721440017

[99] L. Beirão da Veiga, F. Brezzi, L. D. Marini, Virtual elements for linear elasticity problems, SIAM Journal on Numerical Analysis 51 (2) (2013) 794–812.

[100] M. Marino, B. Hudobivnik, P. Wriggers, Computational homogenization of polycrystalline materials with the virtual element method, Computer Methods in Applied Mechanics and Engineering 355 (2019) 349 – 372. doi:https://doi.org/10.1016/j.cma.2019.06.004.
URL http://www.sciencedirect.com/science/article/pii/S0045782519303445

[101] M. Lo Cascio, A. Milazzo, I. Benedetti, Virtual element method for computational homogenization of composite and heterogeneous materials, Composite Structures 232 (2020) 111523.

[102] M. Lo Cascio, M. Grifò, A. Milazzo, I. Benedetti, Computational homogenization of heterogeneous materials by a novel hybrid numerical scheme, Journal of Multiscale Modelling 11 (04) (2020) 2050008.

[103] B. Cockburn, Discontinuous galerkin methods, ZAMM - Journal of Applied Mathematics and Mechanics / Zeitschrift fÃijr Angewandte Mathematik und Mechanik 83 (11) (2003) 731–754. arXiv:https://onlinelibrary.wiley.com/doi/pdf/10.1002/zamm.200310088, doi:https://doi.org/10.1002/zamm.200310088.
URL https://onlinelibrary.wiley.com/doi/abs/10.1002/zamm.200310088

[104] V. Gulizzi, I. Benedetti, A. Milazzo, A high-resolution layer-wise discontinuous galerkin formulation for multilayered composite plates, Composite Structures 242 (2020) 112137. doi:https://doi.org/10.1016/j.compstruct.2020.112137.
URL https://www.sciencedirect.com/science/article/pii/S0263822320300908

[105] V. Gulizzi, I. Benedetti, A. Milazzo, An implicit mesh discontinuous galerkin formulation for higher-order plate theories, Mechanics of Advanced Materials and Structures 27 (17) (2020) 1494–1508. arXiv:https://doi.org/10.1080/15376494.2018.1516258, doi:10.1080/15376494.2018.1516258.
URL https://doi.org/10.1080/15376494.2018.1516258

[106] I. Benedetti, V. Gulizzi, A. Milazzo, Layer-wise discontinuous galerkin methods for piezoelectric laminates, Modelling 1 (2) (2020) 198–214. doi:10.3390/modelling1020012.
URL https://www.mdpi.com/2673-3951/1/2/12

[107] V. Gulizzi, R. Saye, Modeling wave propagation in elastic solids via high-order accurate implicit-mesh discontinuous galerkin methods, Computer Methods in Applied Mechanics and

Engineering 395 (2022) 114971. doi:https://doi.org/10.1016/j.cma.2022.114971.
URL https://www.sciencedirect.com/science/article/pii/S0045782522002250

[108] A. Milazzo, I. Benedetti, M. Aliabadi, Hierarchical fast bem for anisotropic time-harmonic 3-d elastodynamics, Computers & Structures 96-97 (Supplement C) (2012) 9 – 24. doi:https://doi.org/10.1016/j.compstruc.2012.01.010.
URL http://www.sciencedirect.com/science/article/pii/S0045794912000259

[109] V. Gulizzi, A. Milazzo, I. Benedetti, Fundamental solutions for general anisotropic multi-field materials based on spherical harmonics expansions, International Journal of Solids and Structures 100 (2016) 169–186. doi:10.1016/j.ijsolstr.2016.08.014.

[110] V. Gulizzi, I. Benedetti, A. Milazzo, Spherical harmonics expansion of fundamental solutions and their derivatives for homogeneous elliptic operators, Journal of Multiscale Modelling 08 (03n04) (2017) 1740006. arXiv:https://doi.org/10.1142/S1756973717400066, doi:10.1142/S1756973717400066.
URL https://doi.org/10.1142/S1756973717400066